Powder Technology 383 (2021) 564–583

Contents lists available at ScienceDirect

Powder Technology

journal homepage: www.elsevier.com/locate/powtec

The influence of material and process parameters on powder spreading in additive manufacturing

Mohamad Yousef Shaheen [a,b,*], Anthony R. Thornton [a], Stefan Luding [a], Thomas Weinhart [a]

[a] Multi-Scale Mechanics, Faculty of Engineering Technology, University of Twente, Drienerlolaan 5, 7522 NB Enschede, The Netherlands
[b] Design, Production and Management, Faculty of Engineering Technology, University of Twente, Drienerlolaan 5, 7522 NB Enschede, The Netherlands

ARTICLE INFO

Article history:
Received 15 July 2020
Received in revised form 24 December 2020
Accepted 21 January 2021
Available online 08 February 2021

Keywords:
Additive manufacturing
Laser powder bed fusion
Spreading process
Discrete particle method
Powder layer quality

ABSTRACT

Additive manufacturing (AM) or 3D printing is beginning to mature from a rapid prototyping to an industrial production technology. However, there are still a lot of fundamental questions that must be addressed in order to make this leap forward. There are many different AM technologies; here, we focus on laser powder bed fusion (LPBF).

A key step in LPBF is the initial spreading of the powder layer before it is melted in a solid object, via interaction with a laser. Ideally the powder should be spread as a dense, uniform layer. However, developing a spreading process that can produce a consistent layer, across the wide range of powders used, is a challenge for LPBF manufactures. Therefore, we investigate the influence of materials and process parameters on layer quality.

To perform this study we perform computing simulations using the discrete particle method (DPM), a.k.a. discrete element method. This allows us to define metrics to evaluate the powder layer quality, allowing direct comparisons of different tools and parameters. We emulated the effect of the complex particle shape and surface roughness via rolling resistance and interparticle sliding friction. Additionally we investigated the effect of particle cohesion and type of spreading tool.

We found that all these factors have a major, albeit sometimes surprising influence on the powder layer quality. In particular, more irregular shaped particles, rougher particle surfaces and/or higher interfacial cohesion usually, but not always, lead to worse spreadability. In general, there is a trade-off between material and process parameters. For example, increasing the spreading speed decreases layer quality for non- and weakly cohesive powders, but improves it for strongly cohesive ones. On the other hand, using a counter-clockwise rotating roller as a spreading tool improves the powder layer quality compared to spreading with a blade. For both tools, a unique correlation between the quality criteria uniformity and mass fraction is reported allowing an easily measured experimental value to be related to the layer quality. Finally, we showed that size-segregation occurs during spreading and this effects is able to explain some of our results.

1. Introduction

Laser powder bed fusion (LPBF) is an additive manufacturing (AM) technology. In contrast to subtractive or formative methods, objects are produced from three-dimensional digital models in a layer-by-layer fashion. It offers design flexibility and easy customisation that contributed to its rapid growth and wide utilisation in different industrial sectors [1–3]. Fig. 1 shows a schematic of the process. Parts are produced by spreading successive layers of powder material and solidifying selected parts by partially or fully melting them with a laser [2,4]. The powder spreading process is governed by the geometry, speed and material properties of the spreading tool. In addition, powder feedstock and powder characteristics play a major role for the powder layer quality, which in turn influences the final product properties and quality [5–8].

The discrete particle method (DPM) has been recently used to simulate the spreading process in AM. Despite its computational expense, it is a powerful tool for simulating granular materials and understanding particulate system phenomena that are either inaccessible or difficult to obtain from experiments. Early studies of Herbold et al. [9], Mindt et al. [10] and Parteli et al. [11] have used DPM to simulate the spreading process in LPBF. For example, Mindt et al. [10] investigated the influence of the blade gap height: the distance between the powder bed or base plate and the spreading blade, on the spread layer of spherical Ti-6Al-4V powder. They concluded that a blade gap height equal to or less than the maximum particle diameter would result in a reduced packing density. While Parteli et al. [11] simulated the spreading of PA12

* Corresponding author at: Multi-Scale Mechanics, Faculty of Engineering Technology, University of Twente, Drienerlolaan 5, 7522 NB Enschede, The Netherlands.
E-mail addresses: m.y.shaheen@utwente.nl (M.Y. Shaheen), a.r.thornton@utwente.nl (A.R. Thornton), s.luding@utwente.nl (S. Luding), t.weinhart@utwente.nl (T. Weinhart).

https://doi.org/10.1016/j.powtec.2021.01.058

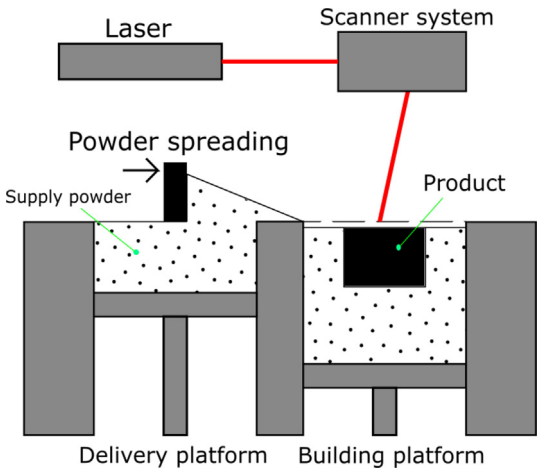

Fig. 1. Laser powder bed fusion (LPBF) process schematic.

powder using a multisphere method to model complex particle shapes with a counter-clockwise (cc) rotating roller as a spreading tool. They showed that the powder bed surface roughness is increased for a higher spreading speed and for powders with a wider size distribution. Parteli et al. [11] findings were confirmed by Haeri et al. [12], who used DPM to spread rod-like particles. They found a higher surface roughness and smaller volume fractions for increased spreading speed and particle aspect ratios. Another study by Haeri [13] investigated the optimization of the blade spreader geometry and found that using a super-elliptic edge profile would result in a better layer quality than a normal flat edge blade.

The flowability behaviour of spherical 316 L stainless steel particles during the spreading process was investigated by Chen et al. [14]. They used DPM to simulate the process with a blade as a spreading tool. They found that decreasing either sliding or rolling friction would decrease the dynamic repose angle and thus improve flowability. While Nan et al. [15] have reconstructed complex particle shape of 316 L stainless steel powder as a function of particle size. They investigated the period and frequency of transient jamming in powder spreading with a small gap height; they found relationships between particle properties, blade speed and gap height. Later, they studied 316 L stainless steel powder flow [16]. They showed that the mass flow rate through the gap, initially, increases linearly with the gap height until it reaches a limit beyond which the mass flow rate cannot be further increased.

Other studies have investigated particle cohesion influence on the spreading process [9,17]. For instance, Meier et al. [17] introduced a DPM model for cohesion and were able to predict the effective surface energy of Ti-6Al-4V. Then they performed a parametric study, highlighting the effect of cohesion on the spreading process. They found that powder layer quality decreases as particle size decreases i.e. cohesiveness increases [18]. Later, Han et al. [19] adapted the approach of Meier et al. [17] to calibrate the surface energy of Hastealloy X (HX) alloy. They found that a layer thickness of 40 μm produce a uniform powder bed spreading.

Recently, Chen et al. [20] investigated 316 L stainless steel powder layer packing density using a blade as a spreading tool. They found that there is a "stress-dip" region at the bottom front of the spreader, and identified three mechanisms that affect the packing density of the powder layer: (1) The "cohesion effect" causes particle agglomerates, (2) the "wall effect" creates vacancies in the powder layer and (3) the "percolation effect" leads to particle segregation. While Fouda et al. [21] performed a DPM simulation of an idealized system with monosized particles using a blade as a spreading tool. They showed that the powder layer packing fraction is always lower than the initial powder heap due to three mechanisms, shear-induced dilation, particle rearrangement and particle inertia.

The "spreadability" of a powder can be defined as the powder ability to spread under certain conditions to form a uniform and highly packed powder layer. Bad spreadability can lead to powder bed defects, segregation, non-uniform density and/or a loose particle packing, all of which have negative effects on the quality of the final product. Unfortunately, powders used in AM tend to behave differently under different conditions. In addition, the recycling of powder changes the material properties, both chemical and morphological ones. Powder properties also depend on powder storage, contamination and environmental effects [5,7,22,23]. Spherical particle shapes are favourable in terms of flowability and powder bed packing density [8]. Fig. 2a shows an SEM image of Ti-6Al-4V powder (produced by plasma rotating electrode) with spherical particles. However, non-sphericity is usually present due to satellites, fractured, adhered particles, etc., as shown in Fig. 3. Fig. 2b shows an example of a Ti-6Al-4V powder (produced by gas atomization) with satellites and wider particle size distribution.[1] The influence of the powder material and spreading process parameters on the spreadability have not been investigated enough in the literature. More specifically, the relationship between particle's shape, surface roughness, cohesiveness and process parameters has not been investigated yet.

In this work we perform a study of the influence of material and process parameters on the spreading process of a Ti-6Al-4V powder, using DPM simulations. The focus is on three material parameters:

(i) The interparticle sliding friction as a measure of surface roughness: we assume that an increase in surface roughness causes a reduction in contact area, and thus an increased normal pressure, which causes plastic deformation of the asperities and thus sliding friction. Fig. 4a shows a schematics of the contact area between two rough solid surfaces. The apparent area A_a is much smaller than the actual contact area A_r, where only the highest asperities are in contact [24]. Fuchs et al. [25] have used nanoindentation to study the rolling, sliding and torsion of micro-sized silica particles. They showed that the measured sliding friction increases as the surface roughness increases.

(ii) Rolling resistance as a simple measure to mimic particle's shape, as an approximation of the behaviour of aspherical particles (resembling small asperities) [24,26,27]. Fig. 4b illustrates how rolling resistance results from the imbalance of the normal reaction force f_n^R at the contact area when an external torque is applied. For example, the rolling behaviour of a polygonal particle can be modelled by a spherical particle with a coefficient of rolling friction $\mu_{r,eq}^{Estrada} = \frac{c}{2R}$ [28], Fig. 4b. Wensrich et al. [27] have demonstrated that a complex particle shape can be captured by rolling friction coefficients of spherical particles, where "a value of around half of the normalised average eccentricity (equivalent rolling friction)" was considered as an appropriate amount to capture the effect of particle shape.

(iii) Effective dry cohesion due to van der Waals interaction, as determined by the interfacial surface energy [9,25,29,30]. Where the standard trick of dry-coating particle surface with nanoparticles is one way to vary cohesion as we do by changing surface energy [31].

The process parameters investigated are the spreading speed and tool geometry. The effect of the gap height and the layer thickness are not considered in this study. A small gap height, and thus a thinner powder layer is usually preferable to achieve higher resolution, i.e., better

[1] Due to the larger particles size distribution, this powder is usually used in electron beam melting (EBM) which is another AM technology that requires powder spreading

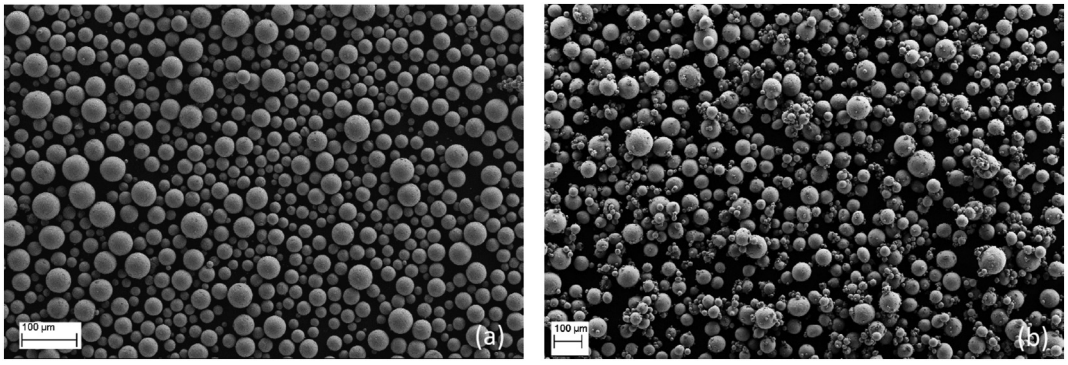

Fig. 2. SEM image of Ti-6Al-4V powders. (a) Ti-6Al-4V powder produced by plasma rotating electrode. $D_{10} = 24\ \mu$m, $D_{50} = 37\ \mu$m, $D_{90} = 56\ \mu$m. (b) Ti-6Al-4V powder produced by gas atomization. $D_{10} = 44\ \mu$m, $D_{50} = 70\ \mu$m, $D_{90} = 107\ \mu$m.

adhesion between constitutive powder layers during the sintering/melting process.

Our parametric study can provide a guidance for the calibration of DPM, showing trends and importance of material and process parameters. A quantitative calibration of the model parameters according to a specific powder material is not performed here. However, we perform a rough calibration to show which parameters result in realistic material behaviour. This is done by measuring the static angle of repose and verify/compare our results with the literature, as a basis of our results on the spread powder layer quality. Fig. 5 shows a flow chart of DPM simulation, calibration and validation framework.

Thus, this paper aims to answer the following questions:

(i) *How to quantify the powder layer quality?*
(ii) *What are the relations between material and process parameters?*
(iii) *What are the effects of particle shape, roughness and cohesiveness on the spread powder layer quality for different process parameters?*

This paper is divided into four more sections. In Section 2, we introduce the methods used, e.g. the DPM force law, the simulation setup, the calibration, etc. We then present and discuss the results in Section 3, before we conclude in section 4.

2. Methods

In Section 2.1, we introduce the force law used in the DPM. The exact DPM parameters used are detailed in Section 2.2. Then we describe the simulation setup in Section 2.3. In Section 2.4, we illustrate the design of the parametric study. We present a preliminary calibration in section 2.5. Finally, we define metrics to characterise the powder layer in Section 2.6.

2.1. Discrete particle method

The discrete particle method is used to simulate the spreading process. The interaction of N poly-disperse particles is modelled using the standard linear spring-dashpot model [32] for the normal force. The normal force (parallel to $\mathbf{r}_{ij}$) is composed of a linear elastic, linear dissipative and a linear adhesive force:

$$f_{ij}^{\mathrm{n}} = k_{\mathrm{n}}\delta_{ij}^{\mathrm{n}} + \eta_{\mathrm{n}}\dot{\delta}_{ij}^{\mathrm{n}} + f_{ij}^{\mathrm{adh}}, \tag{1}$$

with a normal spring stiffness k_{n}, damping coefficient η_{n}, normal relative velocity $\dot{\delta}_{ij}^{\mathrm{n}}$ and a linear adhesion force f_{ij}^{adh}. Each pair of particles i and j are in contact, if their overlap δ_{ij}^{n} is positive. In addition, particles can interact with the base or the powder bed and the spreading tool, which is constructed from polygonal shapes.

Many models exist in DPM to describe dry cohesion of small particles, the attractive force due to van der Waals interaction between particles close to each other or in contact. For simplicity, a linear elastic adhesive force law (acting opposite to the normal elastic repulsive force) is used, which was shown to yield the same bulk rheology as more complicated, more realistic non-linear models [33]:

$$f_{ij}^{\mathrm{adh}} = \begin{cases} -f_{\max}^{\mathrm{adh}} & \delta_{ij}^{\mathrm{n}} \geq 0; \\ -\left(f_{\max}^{\mathrm{adh}} + k_{\mathrm{adh}}\delta_{ij}^{\mathrm{n}}\right) & -\frac{f_{\max}^{\mathrm{adh}}}{k_{\mathrm{adh}}} \leq \delta_{ij}^{\mathrm{n}} < 0; \\ 0 & \text{else}, \end{cases} \tag{2}$$

where k_{adh} is the adhesion "stiffness" during unloading. The maximum adhesion force $f_{\max}^{\mathrm{adh}}$ is defined identical to the pull-off force of the JKR representation of van der Waals interaction [29]: $f_{max}^{\mathrm{adh}} = \frac{3}{2}\pi\gamma(D_{\mathrm{eff}}/2)$, where γ is the surface energy and $D_{\mathrm{eff}} = \frac{D_i D_j}{D_i + D_j}$ is the effective diameter of two particles i and j in contact or close proximity.

The tangential forces (sliding and rolling) are modelled using linear elastic and dissipative forces, where the rolling force is a virtual force, used to calculate the rolling torque. Both the tangential sliding force f^{s} and rolling torque M^{r} are assumed to have a yield criterion, truncating the magnitude of δ^{s} and δ^{r} (the sliding and rolling displacements, respectively) as necessary to satisfy: $|\mathbf{f}^{\mathrm{s}}| \leq \mu_{\mathrm{s}}\,|f_{ij}^{\mathrm{n}} - f_{ij}^{\mathrm{adh}}|$ and $\mathbf{M}^{\mathrm{r}} = (D/2)\,\mathbf{n} \times \mathbf{f}^{\mathrm{r}}$ with $|\mathbf{f}^{\mathrm{r}}| \leq \mu_{\mathrm{r}}\,|f_{ij}^{\mathrm{n}} - f_{ij}^{\mathrm{adh}}|$, where μ_{s} and μ_{r} are the sliding and rolling

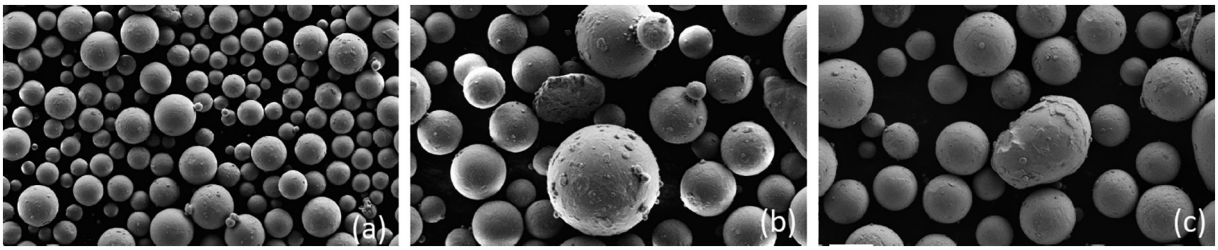

Fig. 3. SEM image of Ti-6Al-4V powder (produced by plasma rotating electrode), showing various types of irregularities. (a) Satellites. (b) Rough surface. (c) Non-sphericity.

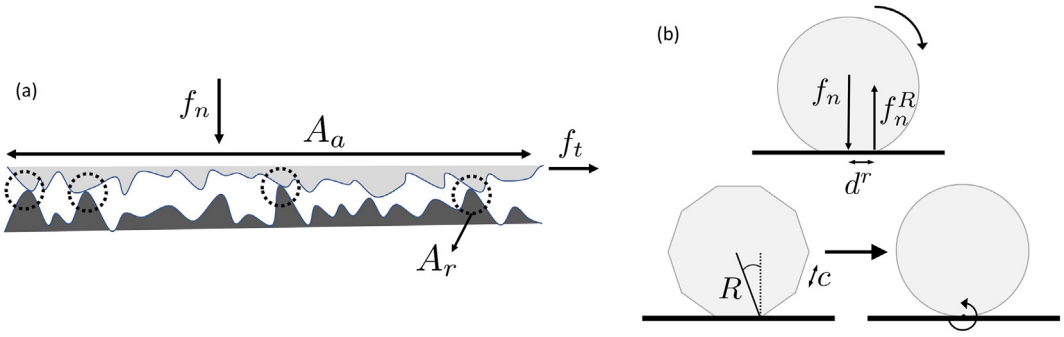

Fig. 4. The physical representation of interparticle sliding and rolling friction. (a) Two rough solid surfaces in contact. (b) The origin of rolling friction and how it can be used to model non-spherical particle shape.

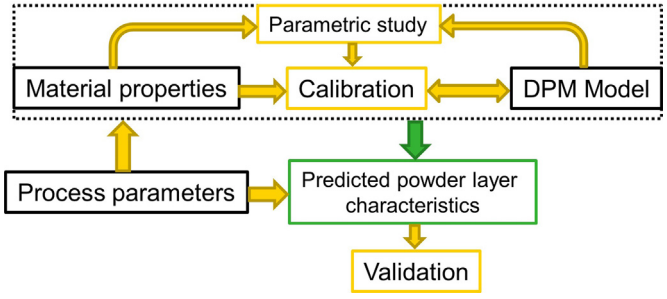

Fig. 5. DPM simulation, calibration and validation framework.

friction coefficients, respectively, usually assumed to be constant (Coulomb type). For the contact model used, the torque scales with the non-cohesive particle diameter for a constant rolling friction coefficient, More details about the contact model can be found in [25,34,35].

2.2. DPM parameters

The simulations of the spreading process are done using the open-source code MercuryDPM [36]. The same parameter values, see Table 1, were set for particle-particle, particle-substrate and particle-tool interactions.

The normal spring k_n and damping η_n constants are set such that the collision time $t_c = t_g/200$ with $t_g = \sqrt{D_{50}/g}$ and an intermediate restitution coefficient of $\varepsilon = 0.4$ (for no adhesion) is assumed. To study the effect of particle surface roughness and sphericity, we simulate the spreading process for varying values of interparticle sliding friction μ_s and rolling friction μ_r, as illustrated in section 2.4. To study the effect of particle cohesion, we simulate the spreading process for varying values of γ such that we can observe a wide range of particle bond numbers. E.g., for $\gamma = 0.1$ mJ/m^2 [17]: $Bo_i = \frac{f_{max}^{adh}}{m_i g} = \frac{9\gamma}{4\rho_p D_i^2 g} \approx 36, 4, 0.8$, for $D_{min} = 12$, $D_{50} = 37$, and $D_{max} = 79\,\mu$m, respectively; This is consistent with the observation that the effect of cohesion is only moderate in the data presented in Section 3 for $\gamma = 0.1$ mJ/m^2 ($Bo_{50} = 4$). The model parameters are set to assure that the interaction is computationally stiff enough i.e. the particle overlap is well below 1% of particle diameter, preventing unrealistic bulk behaviour. Table 1 shows the main DPM simulation parameters.

A log-normal particle size distribution (PSD) is used, fitted to the particle size distribution of Ti-6Al4V. The PSD is measured using laser diffraction with $D_{10} = 24\,\mu$m, $D_{50} = 37\,\mu$m and $D_{90} = 56\,\mu$m. Fig. 6 shows the PSD of Ti-6Al4V as implemented in simulation. It should be noted that we use the real particle size distribution of the powder material i.e. high polydispersity $\frac{D_{max}}{D_{min}} \approx 6.6$, which is not considered previously in the literature, to the best of our knowledge.

2.3. Simulation setup

We simulate a small part of the powder bed (width 1 mm), using periodic boundary condition in y-direction. The spreading tool is a blade (commonly used in AM machines) as shown in Fig. 7, moving from left to right at a constant speed v_T. The substrate is assumed to be smooth. We insert particles in front of the spreader tool, at $(x,y,z) \in [0.5,2.5]$ mm $\times$ [0,1] mm $\times$ [0,h] mm until the total particle volume

Table 1
DPM simulation parameters.

Variable	Symbol	Unit	Value	Values range
Particle density	ρ_p	kg/m^3	4430	–
Normal stiffness	k_n	kg/s^2	2.2	–
Normal dissipation	η_n	kg/s	3.3×10^{-6}	–
Friction stiffness	k_s^t	kg/s^2	$(2/7)k_n$	–
Tangential dissipation	η_s^t	kg/s	$(2/7)\eta_n$	–
Rolling stiffness	k_r^t	kg/s^2	$(2/5)k_n$	–
Rolling dissipation	η_r^t	kg/s	$(2/5)\eta_n$	–
Particle diameter	D_P	μm	–	12–79
	D_{10}	μm	24	–
	D_{50}	μm	37	–
	D_{90}	μm	56	–
Surface energy	γ	mJ/m^2	–	0, 0.1, 0.4
Adhesion stiffness	k_{adh}	kg/s^2	–	$0.5k_n$
Number of particles	N	–	17,169	–
Gap height	H	μm	100	–

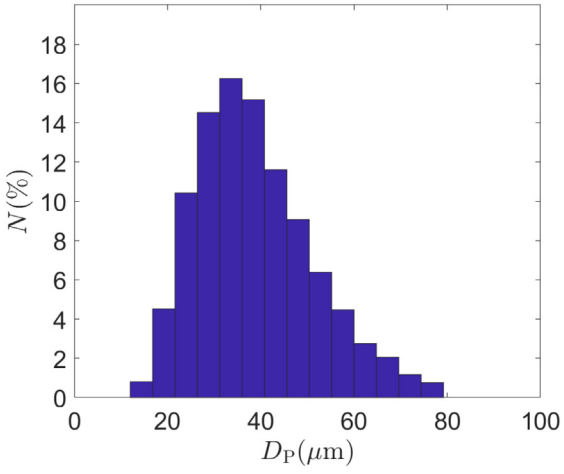

Fig. 6. Particle size distribution of Ti-6Al-4V as implemented in simulation.

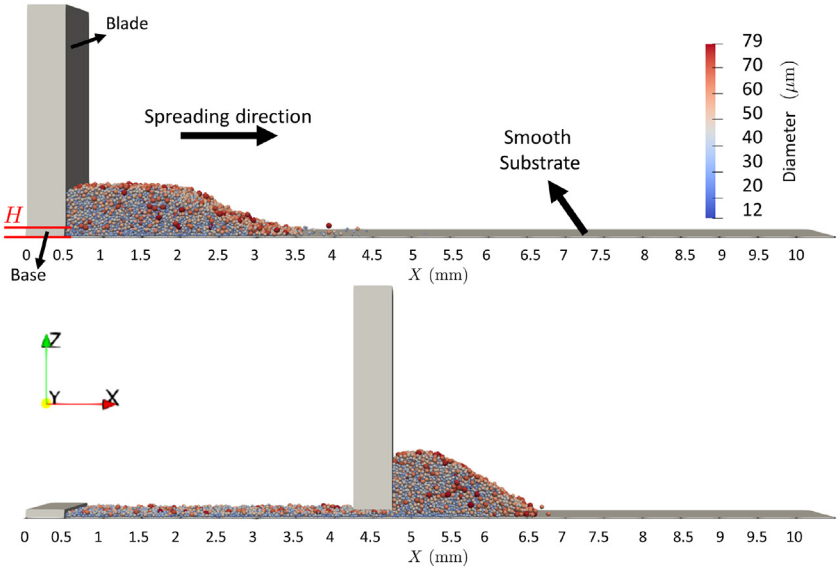

Fig. 7. Simulation setup using a blade as spreading tool with $Bo_{50} = 0$, $\mu_r = 0.1\mu$m, $\mu_s = 0.5\mu$m and $v_T = 10$ mm/s.; color indicates particles diameter.

equals 0.7 mm^3, which is sufficient material to create a powder layer of 7 mm length, 1 mm width and 0.1 mm height. After the particles are settled down and the system is relaxed, the simulation of the spreading process starts by moving the tool at a constant speed v_T. Particles reaching the end of the powder bed (at $x = 10$ mm) get deleted. The simulation ends after spreading the particles in a layer where the tool gap is always set to $H = 100\ \mu$m, which corresponds to about $2.7\times D_{50}$ in z-direction. We stop the simulation at time t_{max} when the system is static i.e. the kinetic energy is very low. Fig. 7 shows the simulation setup, after inserted particles have settled down and during the spreading process.

2.4. Design of simulations

The aim of this study is to find the effect of material and process parameters on the spread powder layer quality. The parameter values considered for the spreading process simulations are shown in Table 2.

The upper limit of the interparticle sliding friction μ_s is chosen to be 0.5, which is realistic for metal powders [37,38]. The rolling friction was varied as a simple measure to mimic particles non-sphericity [26,27] and was varied between 0.005 and 0.4.

The process parameters considered in this study are the spreading tool speed and the spreading tool geometry. The basic spreading tool velocity is chosen to be $v_T = 10$ mm/s, which is low enough such that there are no inertia effects on the bulk behaviour of particles during spreading [18]. Two different spreading tools are considered, a blade Fig. 7 and a counter-clockwise (cc) rotating roller, Fig. 8 similar to the blade setup presented previously in Section 2.3. The roller radius is $r_{roller} = 0.5$ mm and the angular velocity is $w_{roller} = -v_T/r_{roller}$. The gap height is fixed at $H = 100\ \mu$m, such that it is higher than the maximum particle diameter $D_{max} = 79\ \mu$m [10]. The variation of gap height is not considered here, where increasing the gap height will increase the spread layer packing height and fraction [15,16,18].

We use a full factorial design simulating the effect of four variables for two spreading tools geometry, Table 2.

Table 2
Design of simulation parameter study.

Variable	Symbol	Values
Sliding friction coefficient	μ_s	0.5, 0.4, 0.3, 0.25, 0.2, 0.1, 0.05
Rolling friction coefficient	μ_r	0.4, 0.3, 0.2, 0.1, 0.05, 0.005
Bond number	Bo_{50}	0, 4, 15
Spreading tool speed (mm/s)	v_T	10, 50, 100
Spreading tool geometry	–	Blade, cc rotating roller

2.5. Preliminary calibration

A calibration of the DPM model parameters is required to accurately predict the bulk behaviour of a powder material. Here, we have not attempted to match the rolling, sliding friction coefficients and surface energy to any specific Ti-6Al-4V powder material. The current work's aim is to show the qualitative effect of those parameters on the powder layer quality. For an accurate calibration, the particle and contact properties should be chosen to match the static and dynamic angle of repose, the cohesive strength, and the apparent density of the powder material – all tests under low confining stress [39], as relevant for powder spreading. Note that the calibration can be done efficiently by taking advantage of a Bayesian calibration procedure [40].

So far, we have performed only one preliminary calibration measurement: we have simulated a static angle of repose (AOR) test, calculated the AOR, similar to Meier et al. [17] and compared the results to experimental AOR values of Ti-6Al-4V powder material. The simulation setup for measuring the AOR is illustrated in Fig. 9. The opening diameter was set to 0.4 mm and the side length of the square base was set to 1.25 mm. Meier et al. [17] and Han et al. [19] show that the size of the base has only little influence on the measured AOR. For some cases (mostly high frictional) of weakly cohesive particles ($Bo_{50} = 4$), particles did not flow through the 0.4 mm opening, so a larger one of 0.8 mm is used. As most cases of strongly cohesive particles ($Bo_{50} = 15$) did not flow through either the 0.4 mm and 0.8 mm openings, 1 mm one is used instead. However, the highly frictional and strongly cohesive ones did not flow even at 1 mm opening. Fig. 10a, b and c show the numerically measured AOR for $Bo_{50} = 0$, 4 and 15, respectively. We see that the AOR increases as interparticle friction and cohesion increase. The white space in Fig. 10c indicates no-flow.

Meier et al. [17] measured the static angle of repose (AOR) of Ti-6Al-4V powder material for calibration. They have focused on the cohesion effect in terms of the effective surface energy, ignoring the effect of

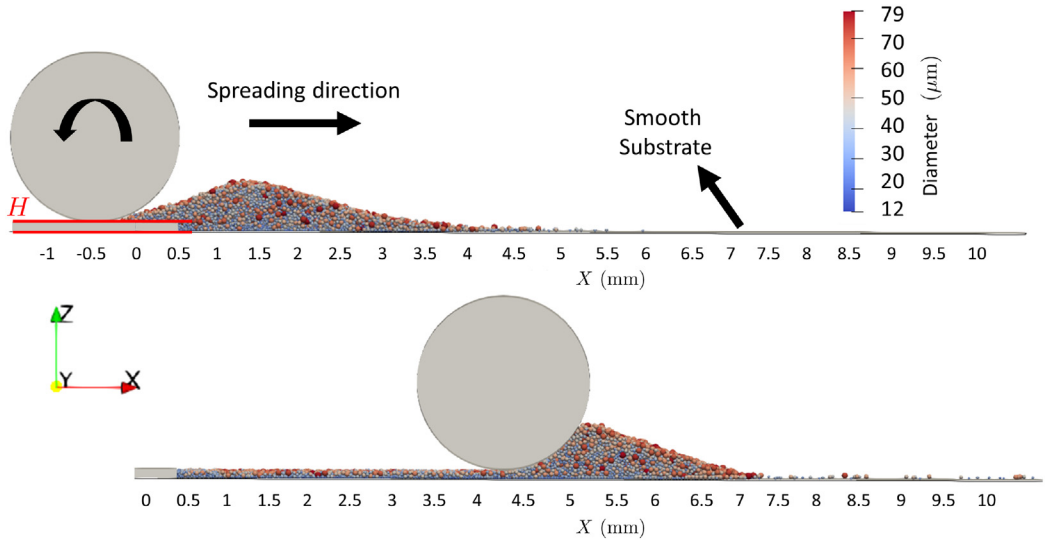

Fig. 8. Simulation setup using a cc rotating roller as spreading tool with $Bo_{50} = 0$, $\mu_r = 0.1\mu$m, $\mu_s = 0.5\mu$m and $v_T = 10$ mm/s.

rolling resistance, only considered rolling dissipation and particle sizes between D_{10} and D_{90} i.e. low polydispersity. Following the same approach for measuring the AOR, including interparticle rolling friction and high polydispersity, we obtain a qualitative comparison with their results. They have found that the AOR is approximately 41° with $\mu_s = 0.4$ and $\gamma = 0.1\,\mathrm{mJ/m^2}$ matches the experimentally measured AOR. This corresponds to our results for the same parameters with approximately $\mu_r = 0.05$, the red circle in Fig. 10b. A top view snapshot of the powder layers with $\mu_s = 0.4$, $\mu_r = 0.05$ and $Bo_{50} = 0$, 4 and 15 are illustrated in Fig. 12a, b and c, respectively. These snapshots show that the results are qualitatively comparable with Meire et al. Fig. 8e, g and h, respectively, [18]. In addition, we have measured the AOR of another Ti-6Al-4V powder material with same PSD used in our simulations, relatively spherical particles shape and some satellite particles [41]. We find that the average measured value of AOR is approximately 44°, Fig. 11. If we assume that the surface energy $\gamma = 0.1\,\mathrm{mJ/m^2}$ and small rolling friction $\mu_r = 0.05$ (since the particles are relatively spherical) then the corresponding sliding friction μ_s is between 0.5 and 0.2, Fig. 10b.

This way we have provided a basic (rough) calibration with two reference Ti-6Al-4V powder materials. We then investigate how the changes in the powder material characteristics will influence the powder layer quality, by varying the values of interparticle friction and cohesion as presented in Section 2.4. Which is one of the main objectives of this paper. It should be noted that AOR is usually used for calibration and powder flowability assessment. However, It is not a sufficient or standalone measure. Powder flowability is one of the terms used to determine powder quality. Although this does not relate directly to powder "spreadability". We discuss further powder "spreadability" assessment and present a simple verification in Section 3.5.

2.6. Powder layer characterisation

In Sections 2.6.1 and 2.6.2, we define two different measures to quantify the powder layer characteristics, namely, mass fraction and uniformity, at the end of the simulation, i.e. after spreading.

2.6.1. Powder layer mass fraction MF

To evaluate the powder layer quality, we define the spread powder layer mass fraction for an assumed volume fraction. Assuming that the layer volume under consideration is $V_{layer} = 7 \times 1 \times 0.1\,\mathrm{mm^3}$, and

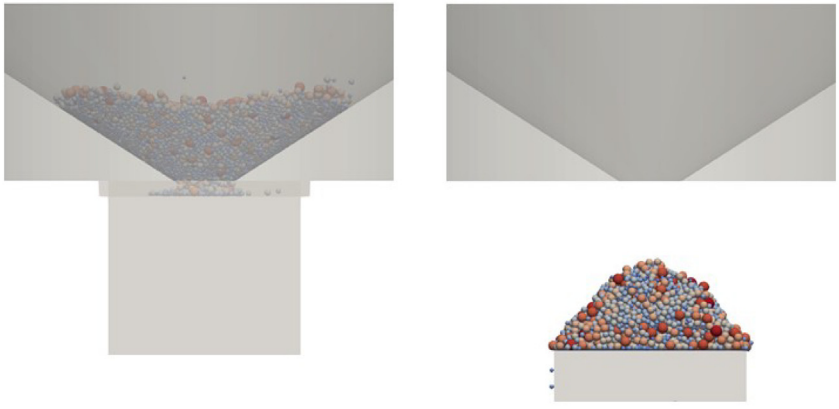

Fig. 9. The simulation setup for measuring the angle of repose. Left: initial configuration, right: final configuration. For $\mu_r = 0.05$, $\mu_s = 0.4$ and $Bo_{50} = 4$.

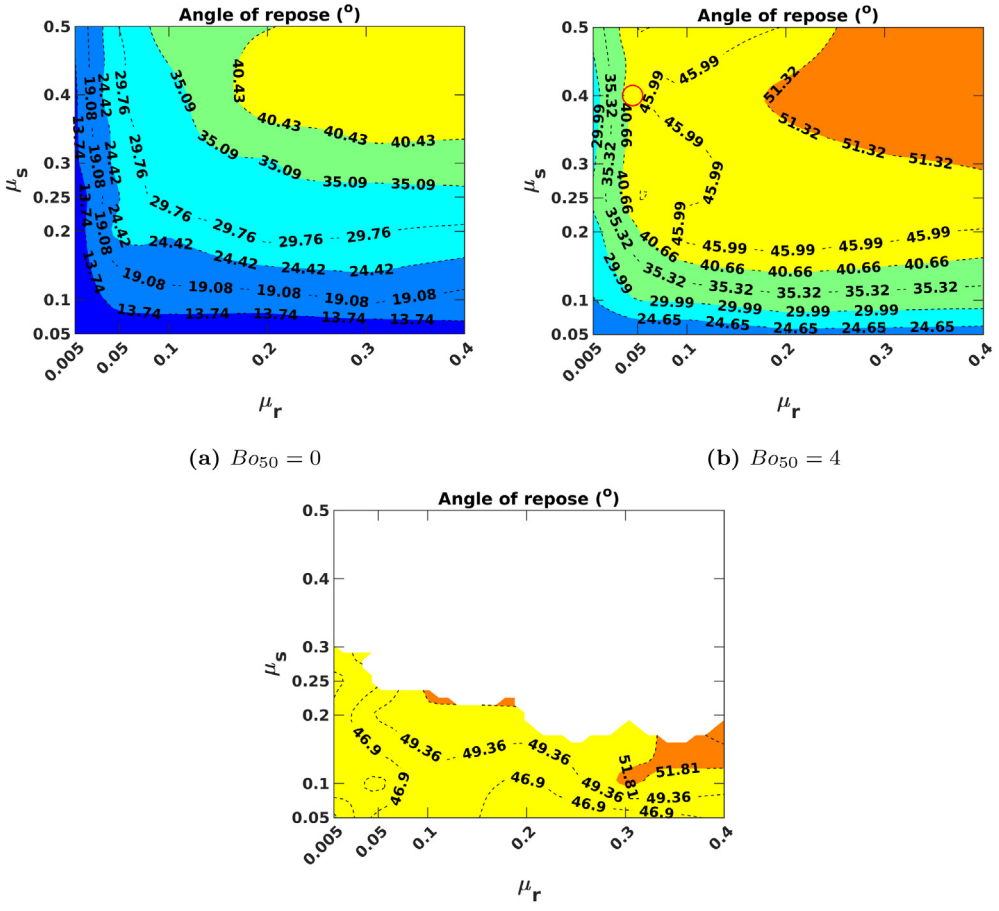

Fig. 10. Contour plots showing the measured angle of repose (AOR) for different values of sliding friction μ_s, rolling friction μ_r and cohesion Bo_{50}.

assuming a theoretical volume fraction $VF = 100\%$, we can calculate the maximum particle mass needed to achieve VF,

$$m_{layer} = VF \times V_{\text{layer}} \times \rho_{\text{p}}, \tag{3}$$

where ρ_{p} is the particle density and $m_{\text{layer}} = 7 \times 1 \times 0.1 \times 10^{-6} \times 4430 = 0.003101$ kg. Then we can define the spread layer mass fraction MF as

$$MF = \frac{m_{\text{SL}}}{m_{\text{layer}}}, \tag{4}$$

where m_{SL} is the total mass of remaining particles after the spreading process within the considered layer volume V_{layer}. It should be noted that the maximum volume fraction that can be achieved is about 64% for random close packing.

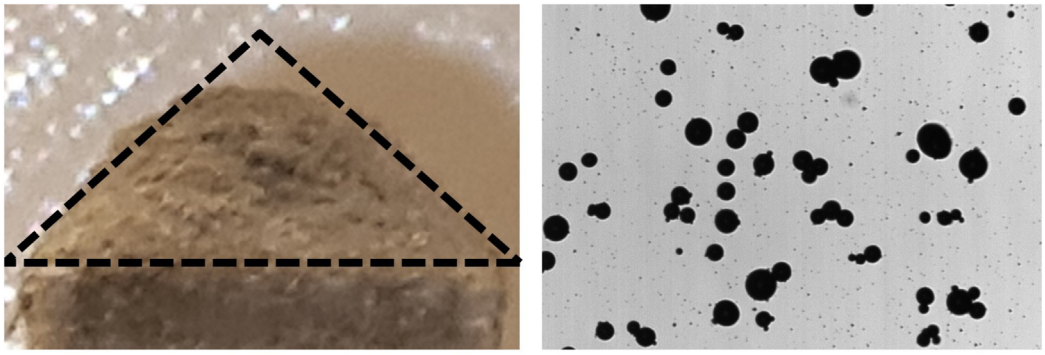

Fig. 11. (a) Experimental funnel result for Ti-6Al-4V powder material with measured angle of repose (AOR) ≈44° and (b) the powder particle shape, illustrating spherical particles with some satellites.

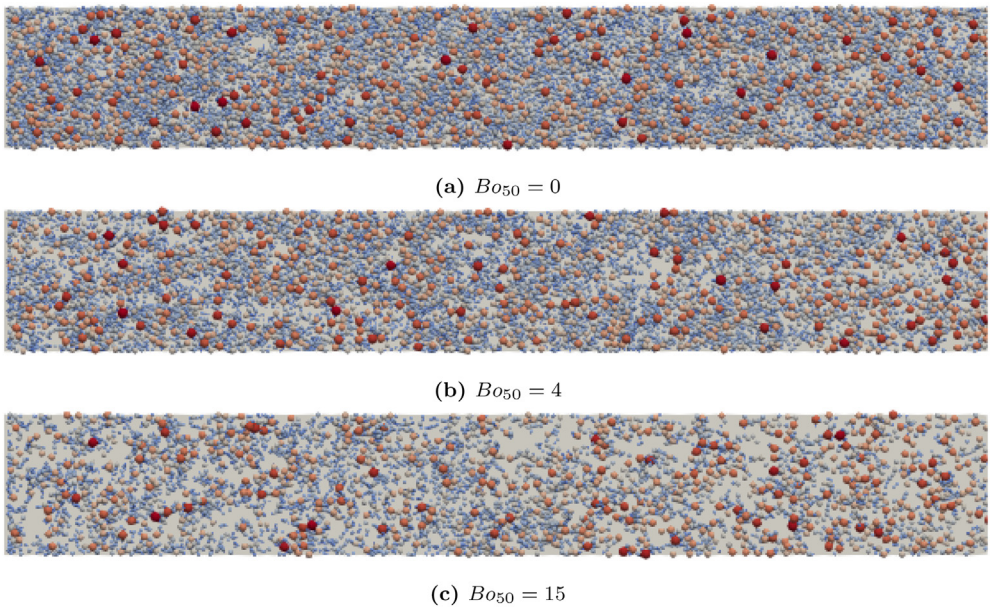

Fig. 12. Top view snapshots of the spread powder layer with $\mu_r = 0.05$ and $\mu_s = 0.4$, using a blade as a spreading tool with v_T= 10 mm/s.

2.6.2. Powder layer uniformity and porosity

We use a micro-macro transition method, coarse-graining (CG) [42], to characterise the spread powder layer uniformity. We extract the solid volume fraction (ϕ) from the discrete data using CG. This method has the advantage that the fields produced satisfy mass and momentum balance exactly even near the boundaries. Here we only use the macroscopic solid volume fraction ϕ after spreading,

$$\phi(x,y,z) = \sum_{i=1}^{N} V_i \psi(\mathbf{r} - \mathbf{r}_i(t_{\max})), \tag{5}$$

where V_i is particle volume. Here, we use a Gaussian coarse-graining function ψ of width (standard deviation) $w = 40\mu$m and a cut-off $w_c = 3w$. The width was chosen to be approximately the maximum particle radius [43]. More details of the CG method are beyond the scope of this paper and the interested reader is referred to [42–44]. Height integration in z-direction yields a spatial distribution field of depth-averaged powder layer solid volume fraction in xy-directions,

$$\overline{\phi}(x,y) = \frac{1}{H}\int_0^H \phi dz, \tag{6}$$

where H is the gap height (here also the expected, optimal layer thickness). The spatial distribution of the depth-averaged solid volume fraction $\overline{\phi}(x,y)$ can be used as a quantitative measure of the powder layer quality and uniformity, as illustrated in the CG figures in Section 3.3. However, we need scalar values for a comprehensive comparison. We define the coefficient of variation (cv) for each $\overline{\phi}(x,y)$ distribution, we obtain a scalar value that can be defined as a measure of spread powder layer uniformity. The coefficient of variation is defined as the ratio of the standard deviation σ to the mean $\mu_{\overline{\phi}}$ of $\overline{\phi}(x,y)$:

$$cv = \frac{\sigma}{\mu_{\overline{\phi}}}, \tag{7}$$

where the mean value $\mu_{\overline{\phi}}$ and standard deviation σ of the solid volume fraction $\overline{\phi}(x,y)$ are defined as

$$\mu_{\overline{\phi}} = \frac{1}{k}\sum_{i=1}^{k} \overline{\phi}(x,y), \tag{8}$$

$$\sigma = \frac{1}{k-1}\sum_{i=1}^{k} \left|\overline{\phi}(x,y) - \mu_{\overline{\phi}}\right|^2, \tag{9}$$

where $k = 100 \times 100$ is the number of sampled (square) grid points in x and y directions, respectively. Non-uniform layers have a high cv, while relatively uniform ones have a low cv. This will be illustrated in

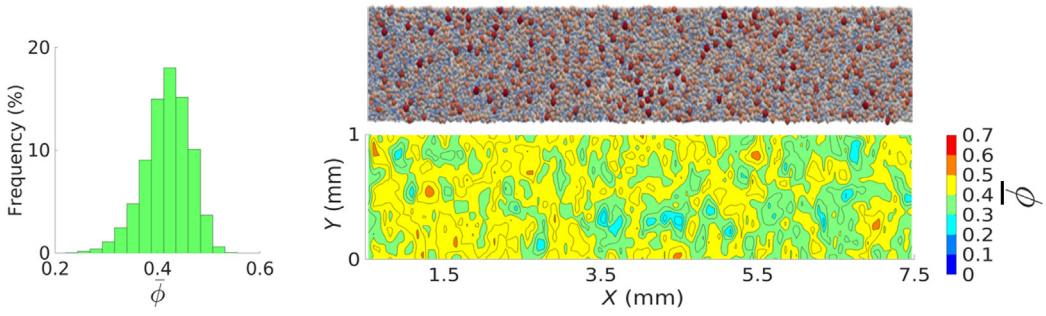

Fig. 13. Snapshot, spatial distribution and probability distribution of the spread powder layer solid volume fraction $\overline{\phi}$ with a blade with $v_T = 10$ mm/s, for weakly cohesive particles $Bo_{50} = 4$ and $\mu_r = 0.005$, $\mu_s = 0.1$. $\sigma \approx 0.04$, $\mu_{\overline{\phi}} \approx 0.4$ and $cv \approx 0.1$.

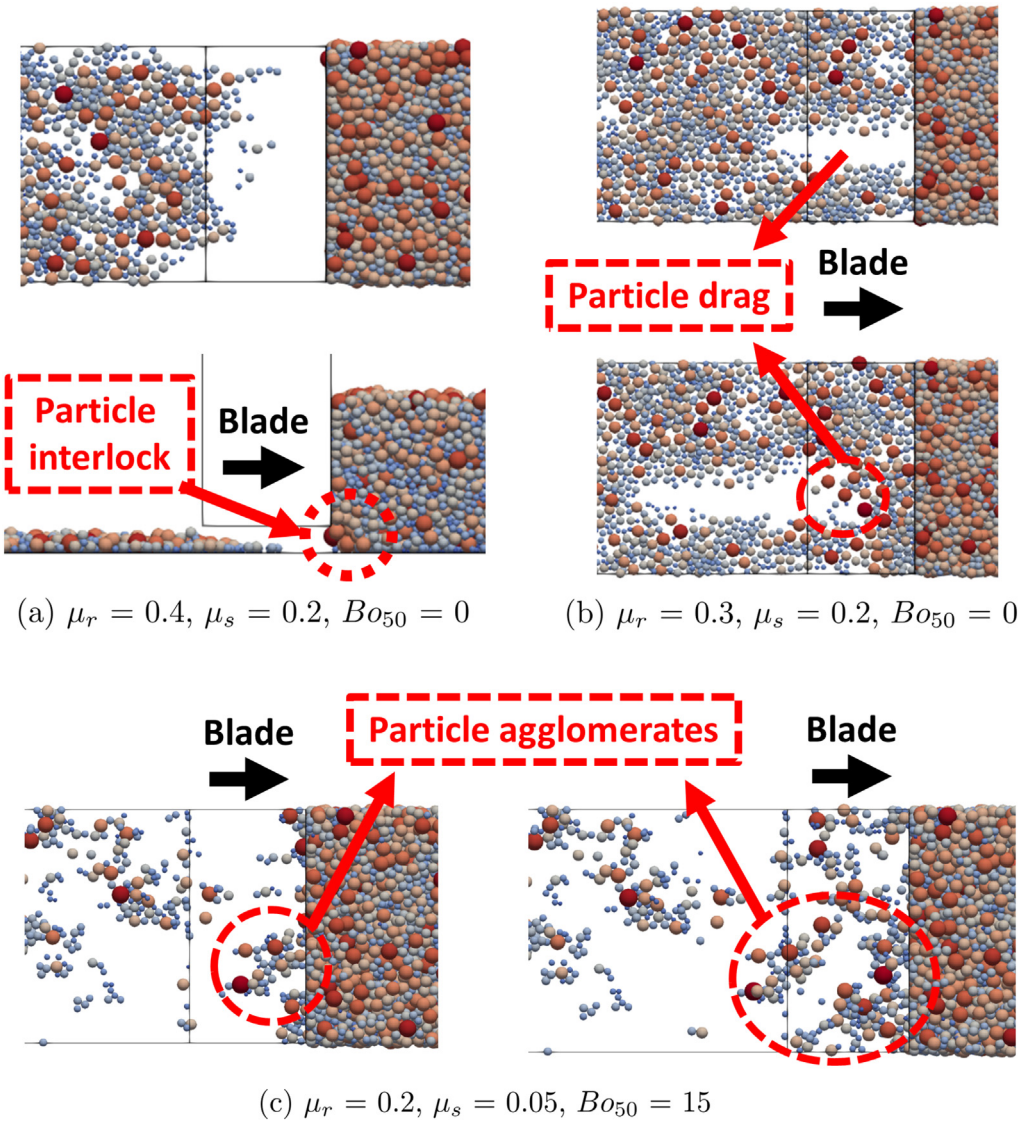

Fig. 14. Spread powder layer defects for a blade. (a) Particle interlock along the whole layer, top and side views. (b) Particle interlock locally (particle drag), top view at $t = 0.29$ s and $t = 0.36$ s, where the interlock caused by large particles broke. (c) Particle agglomerates for strongly cohesive particles.

Section 3.3. Fig. 13 shows an example of the spatial and probability distributions of the solid volume fraction $\overline{\phi}$.

3. Results and discussion

First, we discuss powder layer defects that reduce powder layer quality in section 3.1. Then, we present and discuss the measured powder layer mass fractions *MF* and uniformity *cv* in Section 3.2 and Section 3.3, respectively. We illustrate particle size segregation in Section 3.4. Finally, we present a verification in Section 3.5.

3.1. Spread powder layer defects

We observe several different powder layer defects that affect the powder layer quality, i.e., increase layer porosity. Those defects include empty patches and vacancies, which are caused by particle drag. This occurs when particles are forced forward by the spreading tool, keeping other particles from flowing through the gap. This can either be due to interlocking/clogging for highly frictional (rough) particles, or agglomeration/sticking for strongly cohesive particles. Fig. 14 and Fig. 15 show that particle interlock, particle drag and particle agglomerates occur for both the blade and the counter-clockwise (cc) rotating roller. Whereas strongly cohesive particles stick on both tools, Fig. 15c shows that for the cc rotating roller.

Particle drag during the spreading process was also reported experimentally by Foster et al. [45] and Abdelrahman et al. [46].

3.2. Powder layer mass fraction (MF)

Next, we try to understand the collective effect of three different material parameters on the layer quality, as quantified by the spread layer mass fraction *MF*, for different spreading speeds, using the blade in Fig. 16 or the cc rotating roller in Fig. 17. The major findings and observations are summarized next, while more details are discussed in the following subsections.

The spread layer mass fraction is displayed in Fig. 16 and Fig. 17 for the blade and cc rotating roller, respectively. Each subplot shows the dependence of *MF* on the rolling and sliding friction, accumulating the results of 42 simulations. The plots are arranged in a 3×3 matrix, where each row shows a different speed, $v_T = 10, 50, 100$ mm/s. and each column shows a different mean cohesiveness, $Bo_{50} = 0, 4, 15$. In general, orange indicated very good (close to optimal) layer quality, yellow

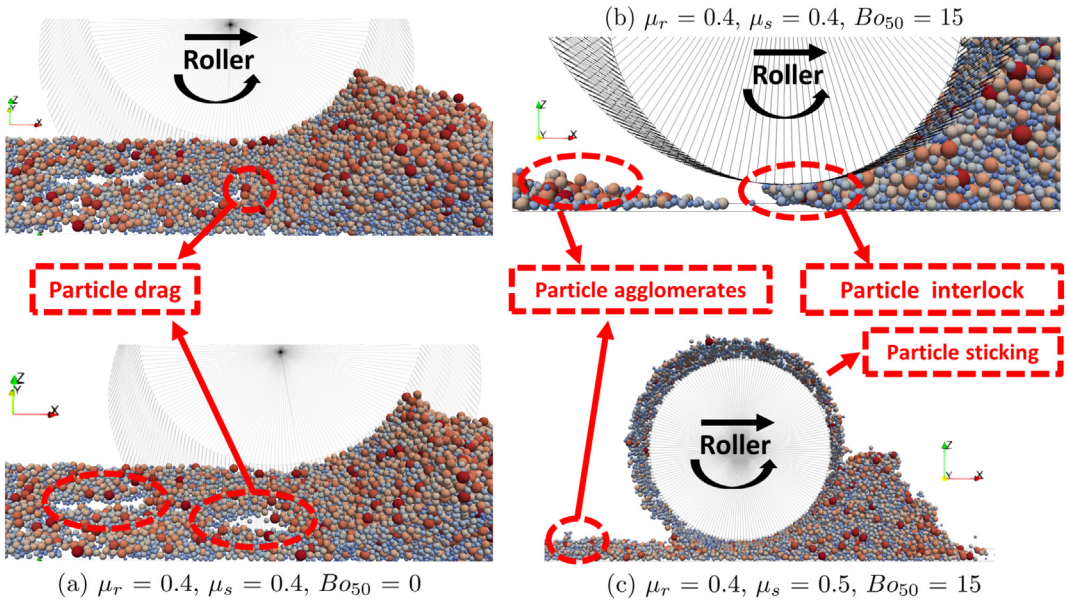

Fig. 15. Spread powder layer defects for a cc rotating roller. (a) Particle drag at two places, side views. (b) Particle interlock and agglomerates. (c) Particle sticking for strongly cohesive particles.

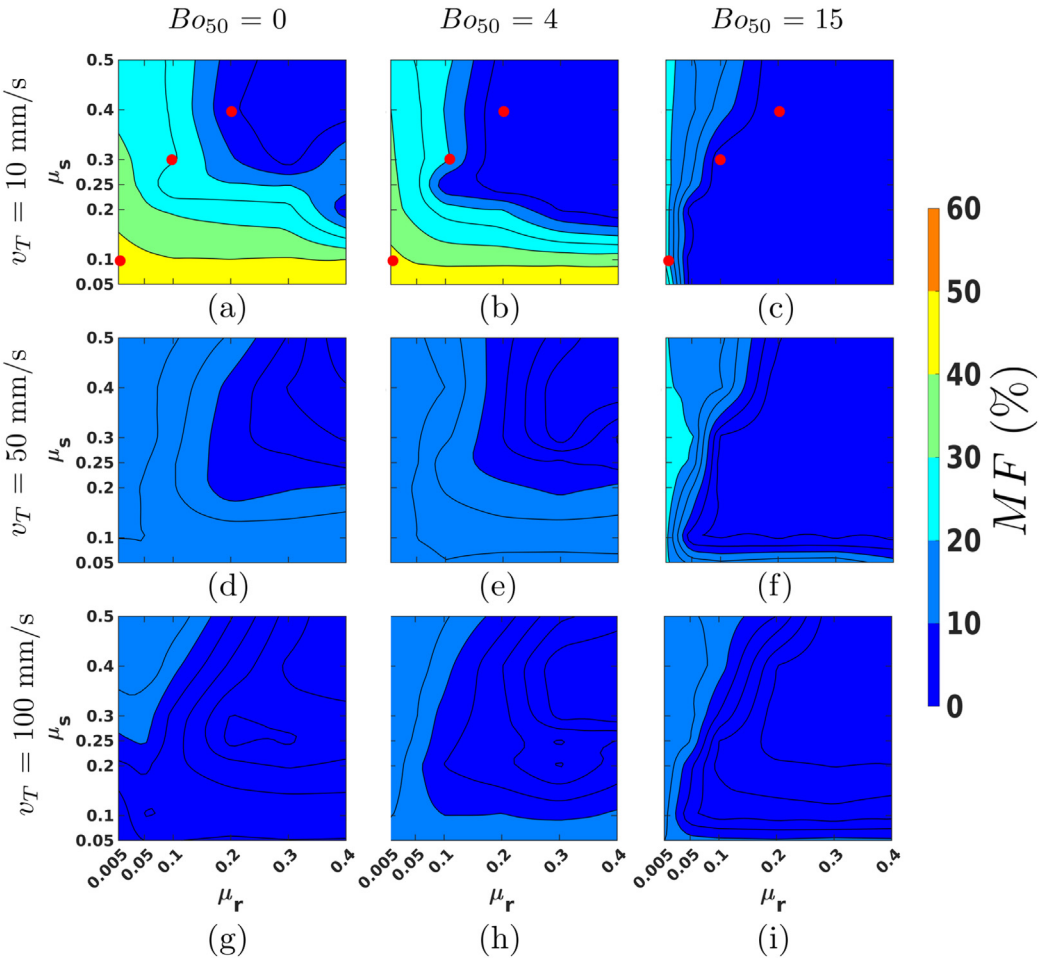

Fig. 16. Spread layer mass fraction MF using a blade as a spreading tool. (a, b, c) $v_T = 10$ mm/s and $Bo_{50} = 0, 4, 15$, (d, e, f) $v_T = 50$ mm/s and $Bo_{50} = 0, 4, 15$, and (g, h, i) $v_T = 100$ mm/s and $Bo_{50} = 0, 4, 15$, respectively. Red dots represent the snapshots in Fig. 18.

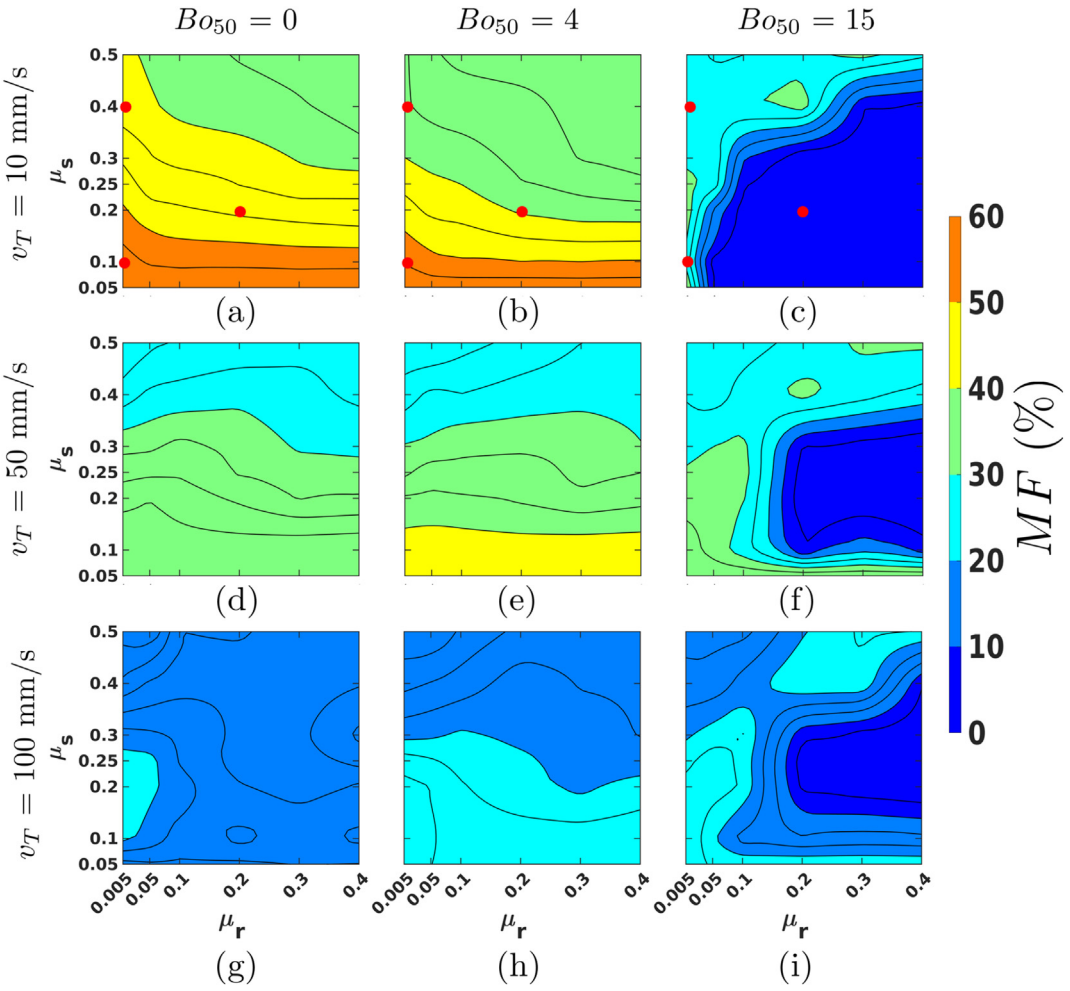

Fig. 17. Spread layer mass fraction *MF* using a cc rotating roller as a spreading tool. (a, b, c) $v_T = 10$ mm/s and $Bo_{50} = 0, 4, 15$, (d, e, f) $v_T = 50$ mm/s and $Bo_{50} = 0, 4, 15$, and (g, h, i) $v_T = 100$ mm/s and $Bo_{50} = 0, 4, 15$, respectively. Red dots represent the snapshots in Fig. 19.

moderate, deteriorating via green and light to dark blue, which indicates very bad layer quality (almost empty layers). Snapshots of several representative examples (indicated by red dot markers in Fig. 16 and Fig. 17) are displayed in Fig. 18 (blade) and Fig. 19 (cc rotating roller).

From this representation – just by looking at the dominant color in a subplot – we can identify parameter combinations that lead to good or bad results in layer quality. Generally, for either tool, we see that as interparticle friction μ_s and μ_r increase, *MF* decreases. For large values of μ_s, an increase in rolling friction, μ_r, decreases *MF*, whereas for small values of μ_s, μ_r has only little influence. In other words, *MF* decreases as particle roughness and non-sphericity increase. In addition, increasing spreading speed typically decreases layer quality and *MF*. Likewise, increasing particle cohesiveness, Bo_{50}, for constant spreading speed, reduces *MF* – with some exceptions, as discussed in detail in Section 3.2.1 for the blade and in Section 3.2.2 for the cc rotating roller. Brika et al. [47] have investigated powder flowability of three different Ti-6Al-4V powders. They concluded that powders with more spherical particles result in higher-quality powder layers, while the presence of fine particles

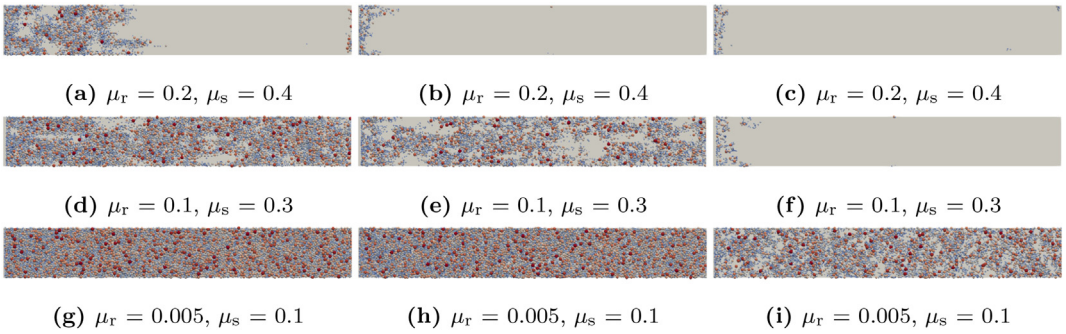

Fig. 18. Top view of the spread powder layer using a blade as a spreading tool at $v_T = 10$ mm/s. (a, d, g) $Bo_{50} = 0$, (b, e, h) $Bo_{50} = 4$ and (c, f, i) $Bo_{50} = 15$. Cases: (a,b,c,f) Empty layers due to global particle drag and particle interlock $MF < 10\%$, (d, e, i) layers with empty patches due to local particle drag $10\% < MF < 30\%$ and (g, h) relatively good dense layers $MF > 30\%$.

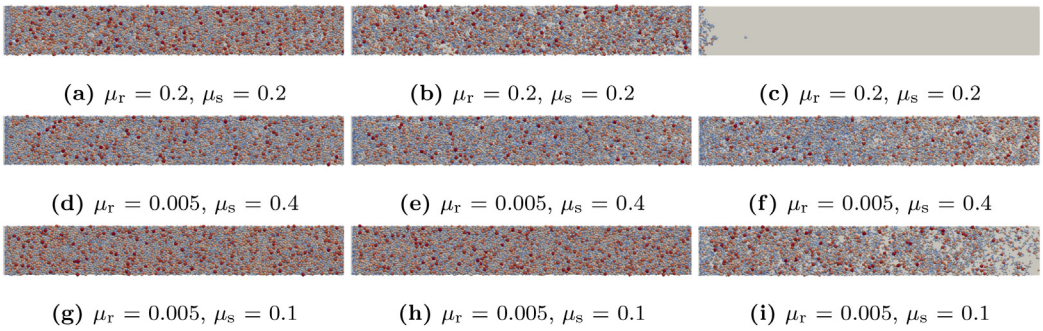

Fig. 19. Top view of the spread powder layer using a counter-clock wise rotating as a spreading tool at $v_T = 10$ mm/s. (a, d, g) $Bo_{50} = 0$, (b, e, h) $Bo_{50} = 4$ and (c, f, i) $Bo_{50} = 15$. Cases: (c) Empty layer due to global particle drag and particle interlock $MF < 10\%$, (b, f, i) layers with empty patches due to local particle drag $10\% < MF < 30\%$ and (a, d, g, e, h) relatively good dense layers $MF > 30\%$.

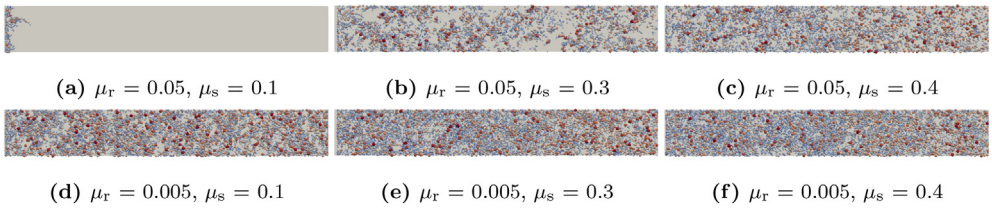

Fig. 20. Top view of the spread powder layer for strongly cohesive particles $Bo_{50} = 15$ using a blade as a spreading tool at $v_T = 10$ mm/s, illustrate the effect of μ_s and μ_r.

reduces layer quality (which contributes to powder cohesion). Similar results were reported by Sutton et al. [48]. They have reviewed common methods used to characterise AM powders and concluded that the presence of agglomerates and irregular particles shape reduce layer quality and uniformity. While Pleass et al. [49] have observed completely empty layers for strongly cohesive particles i.e. no powder was deposited during the spreading process. Where the powder forms a pile and get dragged in front of the spreading blade tool. These conclusions agree well with some of our findings, which will be further discussed in this section.

Comparing the two spreader geometries, unlike the blade tool, the cc rotating roller compacts the powder during the spreading process. This results always in a higher spread layer mass fraction, with MF_{max} of about 60%, while for the blade MF_{max} is only about 50%.

For some cases, e.g., Fig. 16a and Fig. 17a, we see that at low μ_s, as μ_r increases, *MF* is almost unaffected. In contrast, at low μ_r, as μ_s increases, *MF* reduces considerably. This can be related to particle segregation, as will be discussed in detail in section 3.4.

3.2.1. Blade spreader

Zooming into the *MF* results using the blade tool, in Fig. 16, most parameter combinations lead to bad layer quality (small *MF*). Only in Fig. 16a and b yellow/green dominate on bottom and left, whereas in all other subplots *MF* values indicate bad layer quality. This means that the layer quality is better, the smaller the sliding friction and it improves a little for smaller rolling friction. From Fig. 16a, b and c we see that increasing particle cohesiveness from $Bo_{50} = 0$ to 4 barely affects *MF*, while it is deteriorating for strong cohesion, $Bo_{50} = 15$. On the other hand, we obtain relatively high *MF* for non- and weakly cohesive particles ($Bo_{50} = 0, 4$, respectively) in two cases: (i) when particle roughness is relatively low (low μ_s), even for low particle sphericity (high μ_r), (ii) when the particle sphericity is high (low μ_r) even for high particle roughness (high μ_s).

For strongly cohesive particles Fig. 16c, the effect of interparticle friction on *MF* is different. We see that μ_r has a major negative influence on *MF*. However, as μ_s increases, *MF* increases. The reason can be due to the fact that as μ_s increases, contacts between particles decreases reducing the effective cohesion. Similar effects have been previously observed numerically and experimentally. Savkoor et al. [50] have investigated the influence of the tangential forces on adhesive contacts. They concluded that the contact area between particles decreases as the tangential force increases. In addition, Fuchs et al. [25] have used nanoindentation to study the rolling, sliding and torsion of micro-sized silica particles. They showed that, as the surface roughness increases, the sliding friction increases and the sliding adhesion decreases. Fig. 20 show a top view of the spread powder layer for strongly cohesive particles $Bo_{50} = 15$. It illustrates that powder layer quality decreases as μ_s decreases due to particle agglomerates increase.

Fig. 16d, e and f show *MF* for non-, weakly and strongly cohesive particles, $Bo_{50} = 0, 4, 15$, respectively, with spreading speed $v_T = 50$ mm/s. Similarly, Fig. 16g, h and i with spreading speed $v_T = 100$ mm/s. We clearly see that, for non- or weakly cohesive particles, increasing the spreading speed v_T for all cases has reduced the *MF* compared to the lower spreading speed $v_T = 10$ mm/s. MF_{max} is between 30 and 20% at $v_T = 50$ mm/s and $MF_{max} = 20\%$ at $v_T = 100$ mm/s, compared to $MF_{max} \approx 50\%$ at $v_T = 10$ mm/s. Qualitatively, this means increasing spreading speed will reduce layer packing fraction.

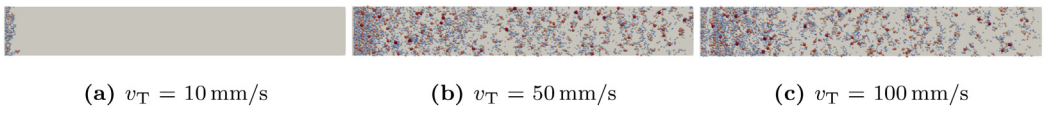

Fig. 21. Top view of the spread powder layer for strongly cohesive particles $Bo_{50} = 15$, $\mu_r = 0.05$ and $\mu_s = 0.05$, using a blade as a spreading tool, illustrate the effect of increasing the spreading speed v_T.

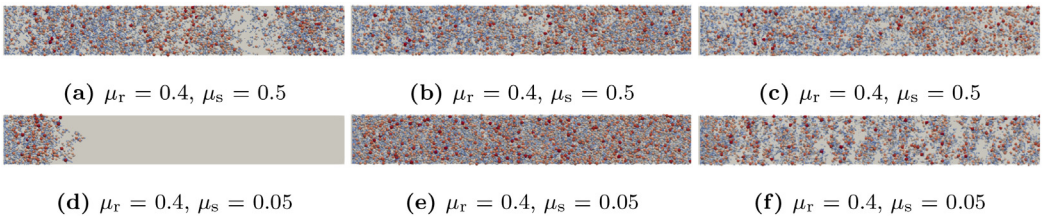

Fig. 22. Top view of the spread powder layer for strongly cohesive particles $Bo_{50} = 15$, using a roller as a spreading tool at (a, d) $v_T = 10$ mm/s (b, e) $v_T = 50$ mm/s (c, f) $v_T = 100$ mm/s, illustrate the effect of increasing the spreading speed v_T.

For strongly cohesive particles, increasing the spreading speed has the opposite effect. *MF* slightly increased at high μ_r and low μ_s compared to the lower spreading speed $v_T = 10$ mm/s, as seen from the contour lines. Fig. 21 show the same effect in a top view of spread powder layer with different spreading speeds $v_T = 10, 50, 100$ mm/s for strongly cohesive particles. A possible explanation is that the high shear rate resulting from higher spreading speed broke the interlocking in front of the spreading tool caused by particle agglomerates and high μ_r, allowing particles to flow.

To provide a basis for the possibility of particle interlocking, we will estimate the range of inertial numbers I, to predict the flow state and the quantify dynamic effects in the system, for two different speeds, as illustrated in Fig. 21a ($v_T = 10$ mm/s) and Fig. 21c ($v_T = 100$ mm/s). The inertial number is defined as

$$I = \frac{\dot{\gamma}\, d_p}{\sqrt{P/\rho_p}}, \tag{10}$$

where d_p is the particle diameter, ρ_p is the particle density, $\dot{\gamma}$ is the shear rate and P is the pressure. Usually three regimes are distinguished: (i) quasi static flow ($I < 10^{-3}$), (ii) dense flow ($10^{-3} < I < 10^{-1}$) and (iii) collisional flow ($I > 10^{-1}$) – however, the boundaries between regimes are not sharp.

First we estimate the inertial number of a single average particle at the free surface:

$$I_D = \frac{\dot{\gamma}\, D_{50}}{\sqrt{\frac{P}{\rho_p}}}, \tag{11}$$

where D_{50} is the average particle diameter, $P_{50} = \frac{m_{50} g}{D_{50}^2}$ is the average single particle pressure, $\dot{\gamma} = \frac{v_T}{H}$ is the shear rate through the gap (assuming homogeneous shear), m_{50} is the average particle mass, g is the gravitational acceleration, v_T is the spreading tool speed and $H = 100\,\mu$m is the rather thin gap height. Larger gaps will only result in smaller $I < I_D$, i.e. an upper limit.

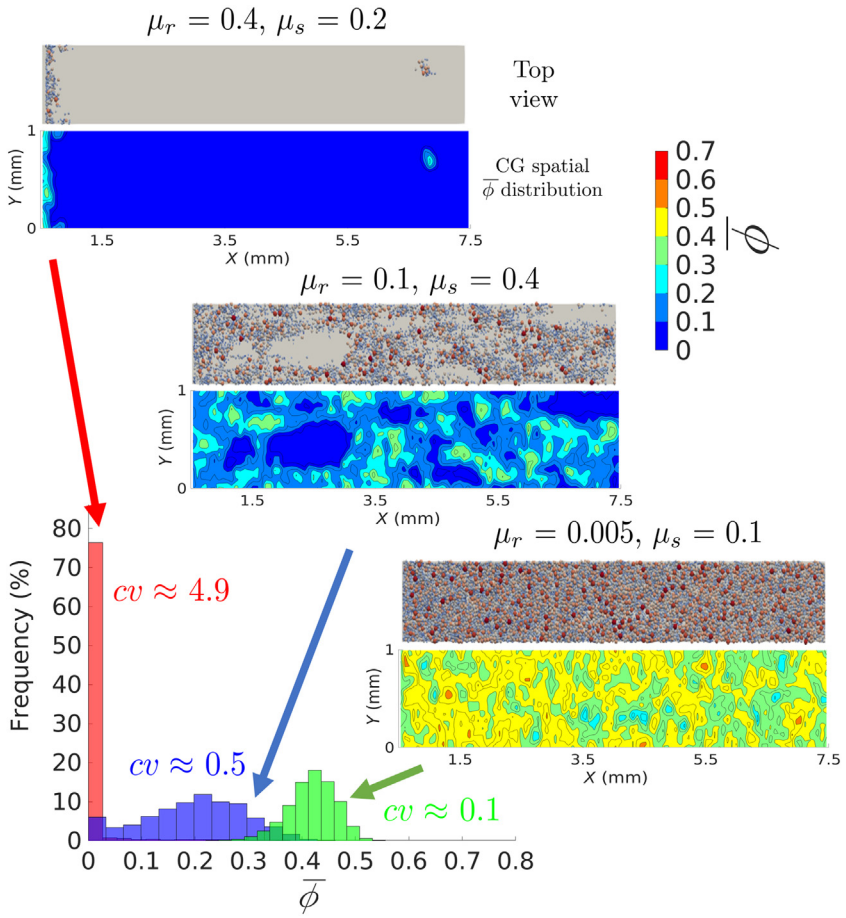

Fig. 23. The spatial and probability solid volume fraction $\overline{\phi}$ distributions of the spread powder layer with a blade at $v_T = 10$ mm/s, for weakly cohesive particles $Bo_{50} = 4$.

Next we estimate the (smaller) inertial number I_{gap} for the base powder layer in the gap (assuming homogeneous shear):

$$I_H = \frac{I_D}{\sqrt{H/D_{50}}}, \tag{12}$$

which is smaller due to the weight of particles, neglecting possible vertical compression effects in the gap due to the tool. Finally, we estimate the inertial number I_Z of the particles under the pile (with height Z_{pile}) in front of the spreading tool, in a thin shear zone of thickness $\propto H$, at the bottom of the pile:

$$I_Z = \frac{I_D}{\sqrt{Z_{pile}/D_{50}}}, \tag{13}$$

due to the weight of the particles in the pile. Since the shear rate in the bulk is typically even smaller, I_Z resembles an upper limit estimate for the bulk.

If the slip layer at the base, as observed in some cases, is localized (thickness $\propto D_{50}$), the estimate would be $I > I_Z$ (not shown), so that I_Z represents the lower limit for particles within, and close to, the gap.

For $v_T = 10$ mm/s: $I_D^{10} = 0.2684$, $I_H^{10} = 0.1633$ and $I_Z^{10} = 0.0660$.
For $v_T = 100$ mm/s: $I_D^{100} = 2.6839$, $I_H^{100} = 1.6326$ and $I_Z^{100} = 0.5482$.
Comparing the lower limits, $I_Z^{10} = 0.0660 < I_Z^{100} = 0.5482$, we conclude that for the lowest spreading speed ($v_T = 10$ mm/s), one could expect dense flow particle interlock, but not for the more dynamic flow state at the highest spreading speed ($v_T = 100$ mm/s), where inertia effects can destroy particle interlock.

Not considered in this estimate is the effect of larger gap heights that will strongly reduce the possibility for interlocking, whereas material parameters like friction and cohesion will work in favor of particle interlock in the gap. In the bulk of the pile, the inertial numbers can be much smaller, $I \ll I_Z$, due to very small, possibly vanishing shear rates in the dense flow state. In fact, inside the bulk, we either observe circular (slow) flow patterns, or completely blocked solid-like piles (field data not shown in this paper).

3.2.2. Roller spreader

Simulations with the cc rotating roller (Fig. 17) generally show a higher *MF* than simulations with the blade spreader. However, the main qualitative dependencies on the material properties remain the

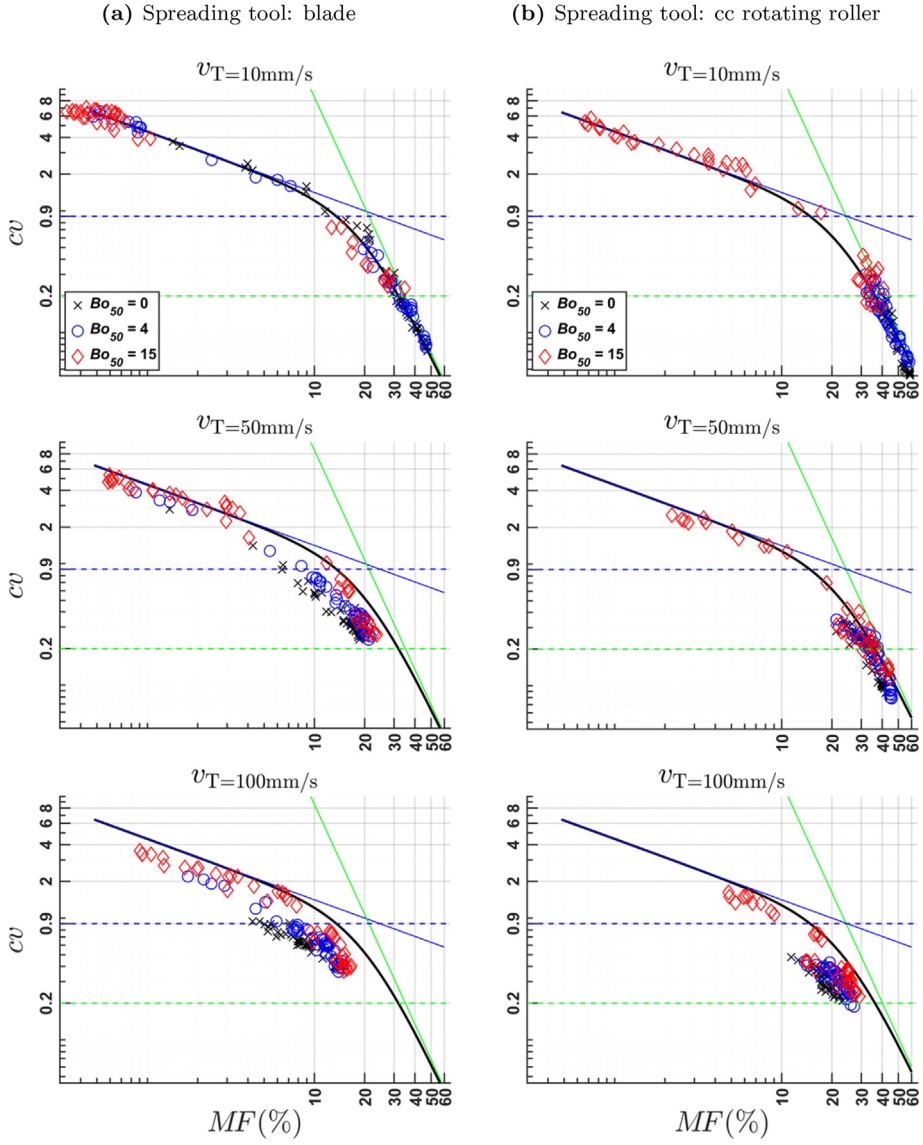

Fig. 24. The correlation between *cv* and *MF*. The *dashed green* and *blue horizontal lines* represent the layer uniformity, cv_u, and vacancies, cv_m, limits, respectively. The *solid black curve* represent the fitting function given by Eq. (14), for parameters see main text. The *solid blue* and *green lines* represent the power laws in Eq. (14) i.e. the first and second terms, with power laws $p_1 = 0.5$ and $p_2 = 3$, respectively.

same; similar to the blade spreader. Fig. 17a and b show that the interparticle friction effect on *MF* is almost the same for non- and weakly cohesive particles. For strongly cohesive particles Fig. 17c, we also see similar behaviour as a blade spreader, low sphericity (high μ_r) has major negative influence on *MF*. As for the blade, *MF* increases as μ_s increases; however, the effect is much more pronounced: at the highest values of μ_s and μ_r, a higher spread layer mass fraction *MF* is obtained, compared to the case for a blade spreader.

Fig. 17d and e show *MF* for non- and weakly cohesive particles, respectively, at $v_T = 50$ mm/s. Similarly, Fig. 17g and h at $v_T = 100$ mm/s. We see lower values of *MF* for almost all cases compared to lower spreading speed at $v_T = 10$ mm/s. Unlike the case of the blade spreader, we see a higher dependency on μ_s than on μ_r at $v_T = 50$ mm/s. Beside that at low μ_s, *MF* is higher for weakly cohesive particles compared to non-cohesive ones; which can be seen at $v_T = 100$ mm/s as well. It seems that the combined effect of particle cohesiveness and roller compaction allowed particles to adhere better to each other and to the substrate, compared to non-cohesive particles.

Fig. 17f and i show *MF* for strongly cohesive particles at spreading speed $v_T = 50$ and 100 mm/s, respectively. At high μ_r and low μ_s, increasing the spreading speed v_T has significantly increased *MF* compared to lower $v_T = 10$ mm/s. Surprisingly, *MF* increases at the higher limit of interparticle friction μ_s and μ_r compared to intermediate values. This indicates a lower and an upper limit of particle roughness (μ_s value) at which particles sphericity (μ_r value) has an effect on the spread powder layer quality when using a roller. Fig. 22 show top view of spread layer using a roller, illustrating the effect of increasing spreading speed v_T. In addition, there is a waving effect on the spread layer for weakly and strongly cohesive particles at low μ_s when $v_T = 100$ mm/s e.g. Fig. 22f.

3.3. Powder layer uniformity and porosity

Dense, uniform powder layers are required to achieve high quality products with low porosity. Previously, we illustrated layer defects which reduce layer uniformity and increase porosity. In this section, we study the spatial distribution of the powder layer solid volume fraction, $\overline{\phi}(x,y)$, where it is utilized to evaluate powder layer uniformity.

In Fig. 23, we show the solid volume fraction $\overline{\phi}$ for three cases, that are representative of the typical kind of powder layers we obtain after spreading: (i) a uniform layer, (ii) empty patches and (ii) a nearly empty layer. We further plot the probability distribution for each case and determine its coefficient of variation *cv*. The cases shown use a blade spreader at $v_T = 10$ mm/s with weakly cohesive particles, $Bo_{50} = 4$. We see good powder layers with a homogeneous narrow normal distribution at low interparticle friction; as the interparticle friction increases the spread powder layer uniformity decreases, with empty patches indicated by the dark blue regions in the contour plot of $\overline{\phi}$. For very high interparticle friction, the probability distribution shows a high peak at zero. Predictably, we observe the highest coefficients of variation for nearly empty layers, and the lowest for uniform layers; thus, we aim to use the coefficient of variation as a measure of layer uniformity and we will see if and how it correlates with *MF*.

Fig. 24a and b show the correlation between *cv* and *MF*, for a blade and a cc rotating roller, respectively. Each row shows one spreader velocity, increasing from top to bottom. The value of $cv_u = 0.2$ is set as an upper limit for a uniform layers. For increasing $cv > cv_u$ the layer uniformity decreases, where layer vacancies and empty patches occur, up to the upper limit of $cv_m = 0.9$; for $cv > cv_m$, we see severe particle interlock and drag causing empty layers. In Fig. 24, we see that the data for different Bo_{50} accumulate on a master curve, sometimes well above the

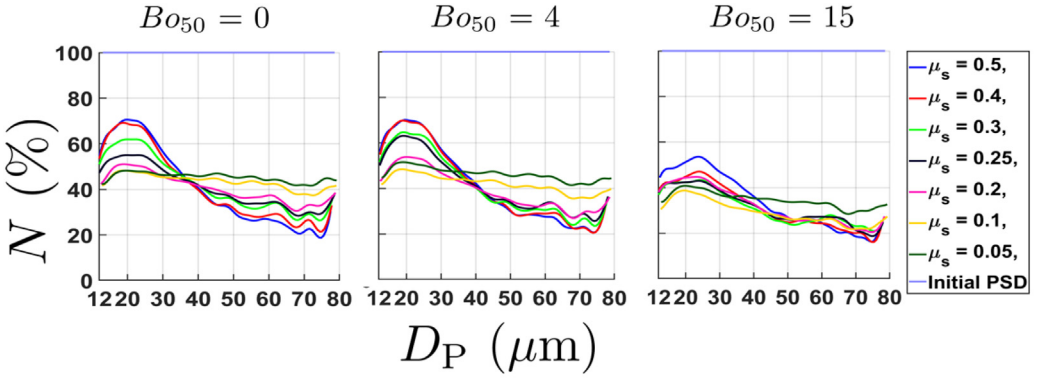

(a) Fixed $\mu_r = 0.005$ and varied μ_s

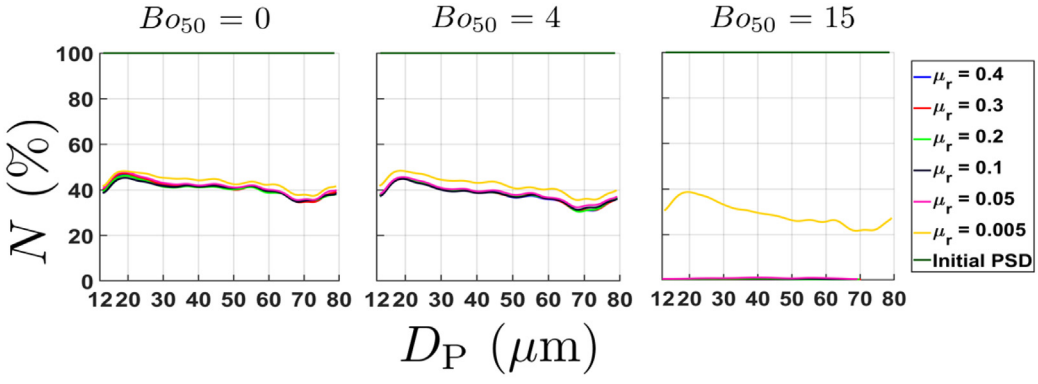

(b) Fixed $\mu_s = 0.1$ and varied μ_r

Fig. 25. Spread powder layer particle size distribution using a blade as a spreading tool at $v_T = 10$ mm/s. From left to right, particle cohesiveness $Bo_{50} = 0$, 4, 15, respectively.

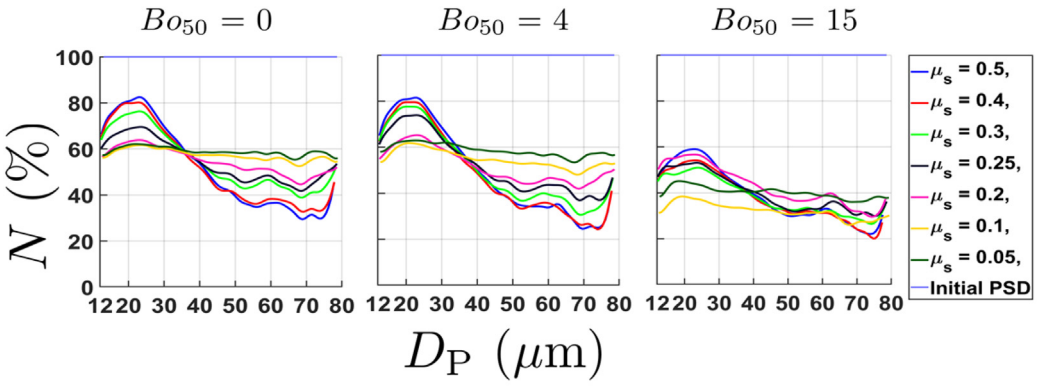

(a) Fixed $\mu_r = 0.005$ and varied μ_s

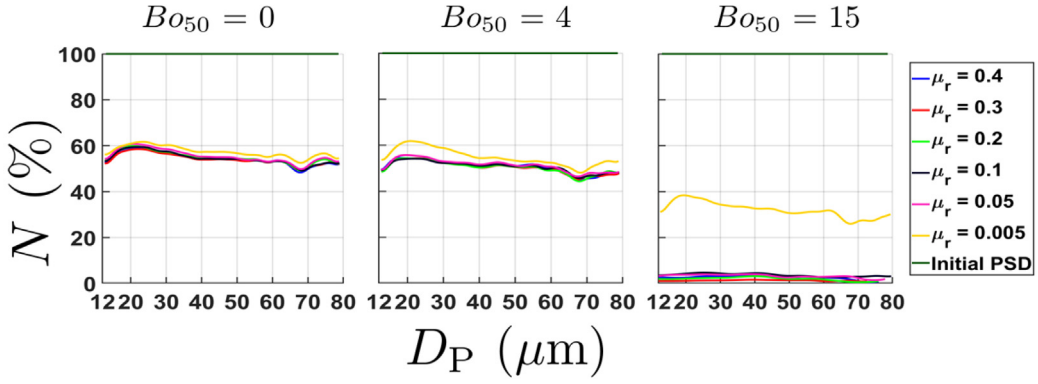

(b) Fixed $\mu_s = 0.1$ and varied μ_r

Fig. 26. Spread powder layer particle size distribution using a cc rotating roller as a spreading tool at $v_T = 10$ mm/s. From left to right, particle cohesiveness $Bo_{50} = 0, 4, 15$, respectively.

upper, in between, or well below the lower limits. The former case are bad packings, whereas the latter are the good quality layers.

Thus, we propose the following function to fit the data for a blade and cc rotating roller at $v_T = 10$ mm/s

$$cv_{\text{fit}} = \left(\left(\frac{MF}{d_1}\right)^{p_1} + \left(\frac{MF}{d_2}\right)^{p_2}\right)^{-1}. \tag{14}$$

First assuming $d_1 = 20$ and $p_1 = 0.5$, which reasonably fits the large $cv > cv_m$ data, we get $p_2 = 3 \pm 0.4$, $d_2 = 20.5 \pm 1$ or $p_2 = 3 \pm 0.2$, $d_2 = 23.5 \pm 1$, for a blade or cc rotating roller, respectively. This master curves fit all these data pretty well and differ only slightly in the d_2 coefficient, meaning that the roller produces slightly better layers with higher MF, or equivalently lower cv. The assumed criteria for d_1 and p_1 result from fitting the data with high $cv \geq cv_m$ (*the solid blue line* in Fig. 24) with the term

$$cv_{\text{fit1}} = \left(\frac{MF}{d_1}\right)^{-p_1} \quad \text{for} \quad cv_{\text{fit1}} \geq cv_m, \tag{15}$$

which gives $d_1 \approx 20$ and $p_1 \approx 0.5$. Then the master curve is assumed as proposed in Eq. (14). *The solid green line* in Fig. 24 is the term

$$cv_{\text{fit2}} = \left(\frac{MF}{d_2}\right)^{-p_2} \quad \text{for} \quad cv_{\text{fit2}} < cv_m, \tag{16}$$

with $p_2 = 3$, $d_2 = 20.5$ or $p_2 = 3$, $d_2 = 23.5$ for a blade or cc rotating roller, respectively.

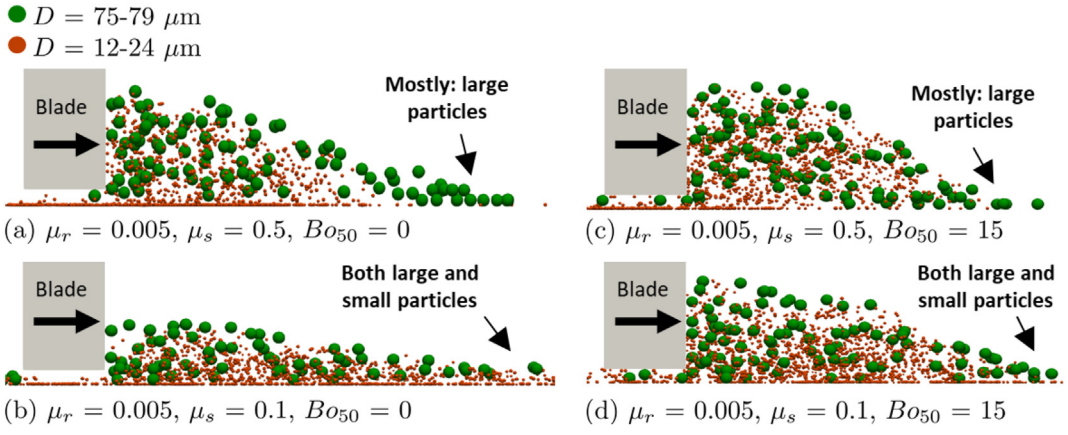

(a) $\mu_r = 0.005$, $\mu_s = 0.5$, $Bo_{50} = 0$

(c) $\mu_r = 0.005$, $\mu_s = 0.5$, $Bo_{50} = 15$

(b) $\mu_r = 0.005$, $\mu_s = 0.1$, $Bo_{50} = 0$

(d) $\mu_r = 0.005$, $\mu_s = 0.1$, $Bo_{50} = 15$

Fig. 27. Side view of powder heap during the spreading process using a blade at $v_T = 10$ mm/s. Illustrating particles segregation at high and low μ_s, for non- and strongly cohesive particles.

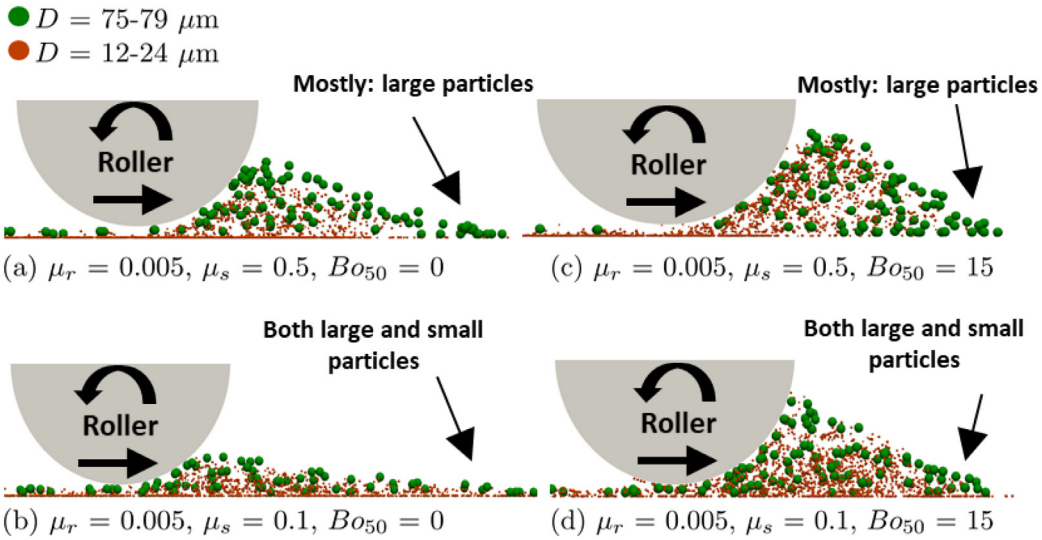

Fig. 28. Side view of powder heap during the spreading process using a cc rotating roller at $v_T = 10$ mm/s. Illustrating particles segregation at high and low μ_s, for non- and strongly cohesive particles.

In more detail, for a blade spreader, Fig. 24a, we see that powder layers with high *MF* are uniform, mostly for non- and weakly cohesive particles, $Bo_{50} = 0$ and 4, respectively. In contrast, for strongly cohesive particles $Bo_{50} = 15$, powder layers either end up close to the low uniformity limit, cv_u, or are of very bad quality. Increasing the spreading speed from $v_T = 10$ mm/s to $v_T = 50$ and 100 mm/s, decreases layer uniformity significantly in almost all cases.

For a cc rotating roller, Fig. 24b, we see similar qualitative results as for a blade spreader when changing the parameters. However, increasing the spreading speed has considerably improved powder layer quality for strongly cohesive particles $Bo_{50} = 15$.

3.4. Particle size segregation

Polydisperse particles segregate when they are in motion. Fig. 25 shows the fraction of particles of a given diameter remaining in the power layer after spreading. I.e., a value of 60% indicates that 40% of the particles have been dragged off the plate by the spreading tool. The data shown is for a blade spreader at $v_T = 10$ mm/s. In Fig. 25a $\mu_r = 0.005$ is fixed and μ_s is varied. While in Fig. 25b $\mu_s = 0.1$ is fixed and μ_r is varied. The columns show different bond numbers, from left to right $Bo_{50} = 0$, 4 and 15, respectively. We can clearly see that, when μ_r is fixed and as μ_s increases Fig. 25a, the retained

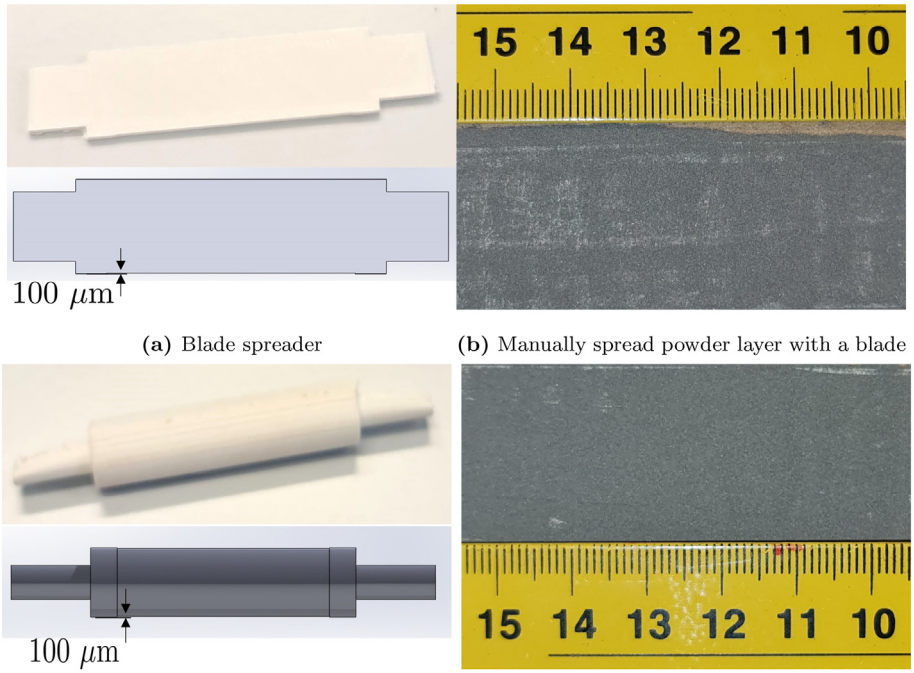

(a) Blade spreader

(b) Manually spread powder layer with a blade

(c) Roller

(d) Manually spread powder layer with a cc rotating roller

Fig. 29. Experimental verification of the powder layer quality. (Left) the tools used in the experiment and (right) the corresponding layers obtained by manually spreading the powder material.

fraction of small particles increases and the retained fraction of large ones decreases, indicating particle segregation (large particles are more likely to be dragged away by the spreader). In the reverse case, when μ_s is fixed and as μ_r increases Fig. 25b, we do not see much difference in the retained particle fraction. Thus, μ_s has larger effect on size-segregation during the spreading process than μ_r. For strongly cohesive particles, the behaviour is similar, but less pronounced, due most likely to the formation of particle agglomerates and a higher dependency of *MF* on μ_r, as mentioned in the previous sections. In addition, It should be noted that the effect of μ_r and μ_s on particle size segregation is comparable for powder layers within the same range of *MF*.

Fig. 27 shows the powder pile during the spreading process with a blade. Only very large (D = 75–79 μm) and very small particles (D = 12–24 μm) are made visible, to be able to see particles migration. Fig. 27a shows the powder pile at low μ_r and high μ_s for non-cohesive particles, we see that mainly large particles are accumulated at the tip of the powder pile. While at low μ_s Fig. 27b, both large and small particles are accumulated at the tip of the powder pile. Similar effect can be seen for strongly cohesive particles Fig. 27c,d, however with less frequency due to particle agglomerates. Similar behaviour is obtained when using a cc rotating roller as a spreading tool, see Fig. 26 and Fig. 28.

3.5. Preliminary verification

Current methods used to assess powder flowability do not relate directly to powder "spreadability" in LPBF. Recently, Cordova et al. [41] have used two wiper blades "applicator tools" designed by the Netherlands Aerospace Centre (NLR) to manually access powder "spreadability" for the applications in LPBF. Both tools have the same blade profile. The first one "open tool" spread the powder pile directly over a metal strip, while in the second tool "funnel tool" the powder is spread through a funnel like shape. They have quantified a thin layer (100μm) quality of four different powder materials and concluded that the "open tool" is better to access the "spreadability" of moisturised powder. In another study, Ahmed et al. [51] have used a simple method to investigate powder layer uniformity. They have spread a powder layer manually with a blade over a glass slide covered by Emery paper. Here, we have also used a simple method to obtain a qualitative comparison of powder layer quality between a blade spreader and cc rotating roller: Powder samples of equal weight were prepared and placed in front of each tool, using a small container box to form a pile of powder. Then the powder was spread manually over a paper tape. The powder used in both experiments is Ti-6Al-4V with measured AOR $\approx 44^{\circ}$. Fig. 29 illustrates the design of those tools and the corresponding layers spread. We see that a cc rotating roller produces a better quality layer than a blade. This shows that same powder material can produce different powder layer quality by changing the process parameter, in this case the spreading tool geometry. Further experiments using same type powder materials (e.g. Ti-6Al-4V) with different characteristics (e.g. particle shape, particle size, etc) will provide more qualitative verification/validation of our simulation results covering a wide range of material parameters that should include many real powder materials.

4. Conclusions

We have simulated the spreading process in AM with the discrete particle method (DPM) and characterized the powder layer quality. We have shown that different powder layer defects can reduce the spread powder layer quality. Those include particle drag, interlock and agglomerates, all of which lead to empty patches that reduce packing fraction, uniformity and thus increase layer porosity. Powder layer defects are more likely to occur due to either high rolling friction, μ_r, high sliding friction, μ_s, strong particle cohesion, Bo_{50}, or the combined effects of those three material characteristics.

When using a blade as a spreading tool, for non- and weakly cohesive particles (Bo_{50} = 0 and 4, respectively), we obtain relatively uniform layers with high layer mass fractions at either low μ_r (even for high μ_s) or low μ_s (even for high μ_r). For strongly cohesive particles (Bo_{50} = 15), μ_r has a major negative influence on layer mass fraction and uniformity, while μ_s has a surprising positive effect: we obtain relatively high layer mass fractions and good uniformity in the limit of low μ_r or high μ_s.

When using a counter-clock wise rotating roller as a spreading tool, better packed and more uniform layers were obtained for almost all cases due to a constructive compression/shear effect. Similar to the blade tool, for strongly cohesive particles at low μ_r or high μ_s, we observe good layer quality.

Increasing the spreading speed has reduced the layer quality for non- and weakly-cohesive particles, for both tools. In contrast, for strongly cohesive particles, the layer quality slightly improved with speed for a blade spreader, but significantly improved for a cc rotating roller.

For both tools, it was shown that μ_s has more influence than μ_r on particle size segregation, which is at the origin of some of the non-intuitive trends we observe.

We have performed a simple experiment to obtain a qualitative comparison of powder layer quality between a blade spreader and counter-clockwise (cc) rotating roller. It was shown that a cc rotating roller provide a better layer quality than a blade.

The present work has provided insight into the combined effects of powder material and process parameters on the spreading process in AM. We did not consider the influence of two process parameters in our current study, namely the gap height and the ambient gas drag, which will be included in future work. Although a comprehensive experimental validation is missing in our current work; nevertheless, we have performed a preliminary calibration and a simple experimental verification.

Further research will focus on experimental calibration and validation of the spreading process for (i) the powder during the process cycle (virgin, used, recycled, etc) and (ii) using the same type powder materials with different characteristics. For calibration, the particle and contact properties should be chosen to match the static and dynamic angles of repose, the cohesive strength, and the apparent density of the powder material – all tests under the relevant low confining stress during spreading. For validation, the mass fraction of the spread powder layer should be measured from experiments and compared with simulations. All this can be done for virgin and re-used particles. Finally, a microscope can be used to investigate the powder layer uniformity, in order to obtain a solid volume fraction distribution, and thus the coefficient of variation. For that purpose, we are developing an experimental setup to accurately control the process parameters and quantify the layer quality.

CRediT authorship contribution statement

Mohamad Yousef Shaheen: Conceptualization, Methodology, Software, Data curation, Visualization, Investigation, Validation, Writing - original draft, Writing - review & editing. **Anthony R. Thornton:** Conceptualization, Writing - review & editing. **Stefan Luding:** Conceptualization, Writing - review & editing. **Thomas Weinhart:** Conceptualization, Funding acquisition, Writing - review & editing.

Declaration of Competing Interest

The authors declare that they have no known competing financial interests or personal relationships that could have appeared to influence the work reported in this paper.

Acknowledgment

This work was financially supported by NWO-TTW project 15050 "Multiscale modelling of agglomeration: Application to tabletting and selective laser sintering". We thank Dr. Laura Cordova for discussions and providing a sample of Ti-6Al-4V powder material.

References

[1] T.D. Ngo, A. Kashani, G. Imbalzano, K.T. Nguyen, D. Hui, Additive manufacturing (3d printing): a review of materials, methods, applications and challenges, Compos. Part B 143 (2018) 172–196.
[2] I. Campbell, D. Bourell, I. Gibson, Additive manufacturing: rapid prototyping comes of age, Rapid Prototyp. J. 18 (2012) 255–258.
[3] W.J. Sames, F. List, S. Pannala, R.R. Dehoff, S.S. Babu, The metallurgy and processing science of metal additive manufacturing, Int. Mater. Rev. 61 (2016) 315–360.
[4] J.P. Kruth, G. Levy, F. Klocke, T.H. Childs, Consolidation phenomena in laser and powder-bed based layered manufacturing, CIRP Ann. Manuf. Technol. 56 (2007) 730–759.
[5] J.H. Tan, W.L.E. Wong, K.W. Dalgarno, An overview of powder granulometry on feedstock and part performance in the selective laser melting process, Addit. Manufact. 18 (2017) 228–255.
[6] W. King, Modeling of Powder Dynamics in Metal Additive Manufacturing: Final Powder Dynamics Meeting Report, 2017.
[7] R.J. Hebert, Metallurgical aspects of powder bed metal additive manufacturing, J. Mater. Sci. 51 (2016) 1165–1175.
[8] S. Vock, B. Klöden, A. Kirchner, T. Weißgärber, B. Kieback, Powders for powder bed fusion: a review, Progr. Addit. Manufact. (2019) 1–15.
[9] E. Herbold, O. Walton, M. Homel, Simulation of powder layer deposition in additive manufacturing processes using the discrete element method, Technical Report, Lawrence Livermore National Lab.(LLNL), Livermore, CA (United States), 2015.
[10] H.W. Mindt, M. Megahed, N.P. Lavery, M.A. Holmes, S.G. Brown, Powder bed layer characteristics: the overseen first-order process input, Metallurg. Mater. Transac. A: Phys. Metal. Mater. Sci. 47 (2016) 3811–3822.
[11] E.J. Parteli, T. Pöschel, Particle-based simulation of powder application in additive manufacturing, Powder Technol. 288 (2016) 96–102.
[12] S. Haeri, Y. Wang, O. Ghita, J. Sun, Discrete element simulation and experimental study of powder spreading process in additive manufacturing, Powder Technol. 306 (2017) 45–54.
[13] S. Haeri, Optimisation of blade type spreaders for powder bed preparation in additive manufacturing using DEM simulations, Powder Technol. 321 (2017) 94–104.
[14] H. Chen, Q. Wei, S. Wen, Z. Li, Y. Shi, Flow behavior of powder particles in layering process of selective laser melting: numerical modeling and experimental verification based on discrete element method, Int. J. Mach. Tools Manuf. 123 (2017) 146–159.
[15] W. Nan, M. Pasha, T. Bonakdar, A. Lopez, U. Zafar, S. Nadimi, M. Ghadiri, Jamming during particle spreading in additive manufacturing, Powder Technol. 338 (2018) 253–262.
[16] W. Nan, M. Ghadiri, Numerical simulation of powder flow during spreading in additive manufacturing, Powder Technol. 342 (2019) 801–807.
[17] C. Meier, R. Weissbach, J. Weinberg, W.A. Wall, A. John Hart, Modeling and characterization of cohesion in fine metal powders with a focus on additive manufacturing process simulations, Powder Technol. 343 (2019) 855–866.
[18] C. Meier, R. Weissbach, J. Weinberg, W.A. Wall, A.J. Hart, Critical influences of particle size and adhesion on the powder layer uniformity in metal additive manufacturing, J. Mater. Process. Technol. 266 (2019) 484–501.
[19] Q. Han, H. Gu, R. Setchi, Discrete element simulation of powder layer thickness in laser additive manufacturing, Powder Technol. 352 (2019) 91–102.
[20] H. Chen, Q. Wei, Y. Zhang, F. Chen, Y. Shi, W. Yan, Powder-spreading mechanisms in powder-bed-based additive manufacturing: experiments and computational modeling, Acta Mater. 179 (2019) 158–171.
[21] Y.M. Fouda, A.E. Bayly, A DEM study of powder spreading in additive layer manufacturing, Granul. Matter 22 (2020) 10.
[22] E. Malekipour, H. El-Mounayri, Common defects and contributing parameters in powder bed fusion am process and their classification for online monitoring and control: a review, Int. J. Adv. Manuf. Technol. 95 (2018) 527–550.
[23] L. Dowling, J. Kennedy, S. O'Shaughnessy, D. Trimble, A review of critical repeatability and reproducibility issues in powder bed fusion, Mater. Des. 186 (2020) 108346.
[24] B. Andreotti, Y. Forterre, O. Pouliquen, Granular Media: Between Fluid and Solid, Cambridge University Press, 2013.
[25] R. Fuchs, T. Weinhart, J. Meyer, H. Zhuang, T. Staedler, X. Jiang, S. Luding, Rolling, sliding and torsion of micron-sized silica particles: experimental, numerical and theoretical analysis, Granul. Matter 16 (2014) 281–297.
[26] C.M. Wensrich, A. Katterfeld, Rolling friction as a technique for modelling particle shape in DEM, Powder Technol. 217 (2012) 409–417.
[27] C.M. Wensrich, A. Katterfeld, D. Sugo, Characterisation of the effects of particle shape using a normalised contact eccentricity, Granul. Matter 16 (2014) 327–337.
[28] N. Estrada, E. Azéma, F. Radjai, A. Taboada, Identification of rolling resistance as a shape parameter in sheared granular media, Phys. Rev. E 84 (2011), 011306, .
[29] K.L. Johnson, K. Kendall, A.D. Roberts, Surface energy and the contact of elastic solids, proceedings of the Royal Society a: mathematical, Phys. Eng. Sci. 324 (1971) 301–313.
[30] O.R. Walton, Review of adhesion fundamentals for micron-scale particles, KONA Powder Particle J. 26 (2008) 129–141.
[31] E. Gärtner, H.Y. Jung, N.J. Peter, G. Dehm, E.A. Jägle, V. Uhlenwinkel, L. Mädler, Reducing cohesion of metal powders for additive manufacturing by nanoparticle dry-coating, Powder Technol. 379 (2020) 585–595.
[32] P.A. Cundall, O.D.L. Strack, A discrete numerical model for granular assemblies, Géotechnique 29 (1979) 47–65.
[33] S. Roy, A. Singh, S. Luding, T. Weinhart, Micro–macro transition and simplified contact models for wet granular materials, Compu. Particle Mech. 3 (2016) 449–462.
[34] S. Luding, Cohesive, frictional powders: contact models for tension, Granul. Matter 10 (2008) 235–246.
[35] T. Weinhart, A.R. Thornton, S. Luding, O. Bokhove, Closure relations for shallow granular flows from particle simulations, Granul. Matter 14 (2012) 531–552.
[36] T. Weinhart, L. Orefice, M. Post, M.P. van Schrojenstein Lantman, I.F. Denissen, D.R. Tunuguntla, J. Tsang, H. Cheng, M.Y. Shaheen, H. Shi, P. Rapino, E. Grannonio, N. Losacco, J. Barbosa, L. Jing, J.E.A. Naranjo, S. Roy, W.K. den Otter, A.R. Thornton, Fast, flexible particle simulations â€ an introduction to MercuryDPM, Comput. Phys. Commun. 249 (2020) 107129.
[37] S. Geer, M.L. Bernhardt-Barry, E.J. Garboczi, J. Whiting, A. Donmez, A more efficient method for calibrating discrete element method parameters for simulations of metallic powder used in additive manufacturing, Granul. Matter 20 (2018) 77.
[38] P.W. Cleary, Dem prediction of industrial and geophysical particle flows, Particuology 8 (2010) 106–118.
[39] H. Shi, G. Lumay, S. Luding, Stretching the limits of dynamic and quasi-static flow testing on cohesive limestone powders, Powder Technol. 367 (2020) 183–191.
[40] H. Cheng, T. Shuku, K. Thoeni, P. Tempone, S. Luding, V. Magnanimo, An iterative bayesian filtering framework for fast and automated calibration of dem models, Comput. Methods Appl. Mech. Eng. 350 (2019) 268–294.
[41] L. Cordova, T. Bor, M. de Smit, M. Campos, T. Tinga, Measuring the spreadability of pre-treated and moisturized powders for laser powder bed fusion, Addit. Manufact. 32 (2020) 101082.
[42] T. Weinhart, A.R. Thornton, S. Luding, O. Bokhove, From discrete particles to continuum fields near a boundary, Granul. Matter 14 (2012) 289–294.
[43] D.R. Tunuguntla, A.R. Thornton, T. Weinhart, From discrete elements to continuum fields: extension to bidisperse systems, Compu. Particle Mech. 3 (2016) 349–365.
[44] I. Goldhirsch, Stress, stress asymmetry and couple stress: from discrete particles to continuous fields, Granul. Matter 12 (2010) 239–252.
[45] B.K. Foster, E.W. Reutzel, A.R. Nassar, C.J. Dickman, B.T. Hall, A brief survey of sensing for metal-based powder bed fusion additive manufacturing, in: K.G. Harding, T. Yoshizawa (Eds.), Dimensional Optical Metrology and Inspection for Practical Applications IV, vol. 9489, International Society for Optics and Photonics, SPIE 2015, pp. 40–48.
[46] M. Abdelrahman, E.W. Reutzel, A.R. Nassar, T.L. Starr, Flaw detection in powder bed fusion using optical imaging, Addit. Manufact. 15 (2017) 1–11.
[47] S.E. Brika, M. Letenneur, C.A. Dion, V. Brailovski, Influence of particle morphology and size distribution on the powder flowability and laser powder bed fusion manufacturability of ti-6al-4v alloy, Addit. Manufact. 31 (2020) 100929.
[48] A.T. Sutton, C.S. Kriewall, M.C. Leu, J.W. Newkirk, Powder characterisation techniques and effects of powder characteristics on part properties in powder-bed fusion processes, Virt. Phys. Prototyping 12 (2017) 3–29.
[49] C. Pleass, S. Jothi, Influence of powder characteristics and additive manufacturing process parameters on the microstructure and mechanical behaviour of inconel 625 fabricated by selective laser melting, Addit. Manufact. 24 (2018) 419–431.
[50] A. Savkoor, G. Briggs, The effect of tangential force on the contact of elastic solids in adhesion, Proce. Royal Soc. London. A. Math. Phys. Sci. 356 (1977) 103–114.
[51] M. Ahmed, M. Pasha, W. Nan, M. Ghadiri, A simple method for assessing powder spreadability for additive manufacturing, Powder Technol. 367 (2020) 671–679.

Mohamad Yousef Shaheen is a PhD candidate at the Multi-Scale Mechanics group at the University of Twente. He is also a member of the MercuryDPM developers team since 2017. He holds a BSc in mechanical engineering and completed his MSc studies as part of the joint Erasmus Mundus MSc program "MathMods", where he obtained a double major MSc degree in mathematical engineering and computational materials science. His PhD research focuses on the numerical and experimental process optimization of laser powder bed fusion (LPBF) technology. He utilizes existing numerical models/tools and develops new ones to predict materials processability for LPBF. He also aims to validated the simulation results with experiments.

Anthony Thornton is an applied mathematician whose research focuses on combined theory, experiments and simulations to model granular systems. He is best known for his work on modelling particle-size segregation in dense granular flows and micro-macro transition methods. He co-founded the open-source simulation code MercuryDPM and his research has applications in many areas including 3D-printing, pharmaceutical, food science, mining, particle technology and geophysics. In 2015 he co-founded the UT spin-off company MercuryLab, whose aim is to make MercuryDPM accessible for industry utilisation and 2017 he gained the title Professor of 'Granular Materials'.

Stefan Luding studied physics until 1990, continued this PhD in Freiburg on simulations of dry granular materials and spent his postdoc in Paris, 1994–1995, before joining Computational Physics in Stuttgart, where he did his habilitation in 1998. In 2001, he moved to TU-Delft in NL as Associate Professor Particle Technology.
Since 2007, he holds the chair Multi-Scale Mechanics, at the University of Twente, with ongoing research on particles, fluids AND solids, granular transitions, powders, etc.
Since 1998 he is Editor of Granular Matter; since 2005 president of AEMMG, organizing Powders&Grains every four years, next: Buenos Aires, Argentinia, July 2021.

Thomas Weinhart is an Associate Professor in the Department of Thermal & Fluid Engineering at the University of Twente. He develops software and material models to simulate granular processes. Anthony Thornton and he founded MercuryDPM, a cutting-edge open-source software for discrete particle simulations. He also developed MercuryCG, a robust and accurate technique to couple micro- and macro-scale models. His research focus is on multi-scale, multi-physics problems such as 3D printing, sintering, tabletting, and agglomeration.